
Masters Theses

Student Theses and Dissertations

Spring 2008

A separation criterion and non-intrusive thickness measurement technique for shear-driven films

Mark A. Friedrich

Follow this and additional works at: https://scholarsmine.mst.edu/masters_theses



Part of the [Mechanical Engineering Commons](#)

Department:

Recommended Citation

Friedrich, Mark A., "A separation criterion and non-intrusive thickness measurement technique for shear-driven films" (2008). *Masters Theses*. 6725.

https://scholarsmine.mst.edu/masters_theses/6725

This thesis is brought to you by Scholars' Mine, a service of the Missouri S&T Library and Learning Resources. This work is protected by U. S. Copyright Law. Unauthorized use including reproduction for redistribution requires the permission of the copyright holder. For more information, please contact scholarsmine@mst.edu.

**A SEPARATION CRITERION AND NON-INTRUSIVE THICKNESS
MEASUREMENT TECHNIQUE FOR SHEAR-DRIVEN FILMS**

by

MARK ALLAN FRIEDRICH

A THESIS

Presented to the Faculty of the Graduate School of the

MISSOURI UNIVERSITY OF SCIENCE AND TECHNOLOGY

In Partial Fulfillment of the Requirements for the Degree

MASTER OF SCIENCE IN MECHANICAL ENGINEERING

2008

Approved by

**James A. Drallmeier, Advisor
Bassem F. Armaly
Ronald A. Kohser**

PUBLICATION THESIS OPTION

This thesis consists of the following two articles that have been submitted for publication as follows:

- Pages 11-44 have been submitted and accepted for publication in the
JOURNAL OF FLUIDS ENGINEERING.
- Pages 45-77 are intended for submission to the journal ATOMIZATION AND
SPRAYS.
- Appendices A, B, C, D, and E have been added for purposes normal to thesis
writing.

ABSTRACT

The behavior of a shear-driven thin liquid film at a sharp expanding corner is of interest in many engineering applications. However, details of the interaction between inertial, surface tension, and gravitational forces at the corner that result in partial or complete separation of the film from the surface are not clear. The focus of this study was to develop a criterion to predict the onset of shear-driven film separation from the surface at an expanding corner as well as to develop a film thickness measurement technique that could be used to obtain an average film thickness for input into the film separation model. The criterion is proposed and is validated with experimental measurements of the percent of film mass separated as well as comparisons to other observations from the literature. The results show that the proposed force ratio correlates well to the onset of film separation over a wide range of experimental test conditions. The correlation suggests the gas phase impacts the separation process only through its effect on the liquid film momentum.

The lack of a reliable, non-intrusive technique to capture and analyze the characteristics of the film limits current efforts to achieve an accurate model of the film flow. An interferometric film thickness measurement technique, along with a Fast Fourier Transform based post-processing method, are presented for use as a diagnostic tool to obtain the average thickness of these shear-driven films with surface instabilities. The approach centers on the concept that one single, unique interferometric fringe spacing will exist over an image with a valid film thickness measurement. Important considerations for accurate measurement of the film thickness are discussed, along with experimental results showing the capability of the technique.

ACKNOWLEDGEMENTS

First, I want to extend my greatest respect and appreciation to my advisor, Dr. James A. Drallmeier, and his expertise as a researcher, mentor, and educator. It is through his guidance, perseverance, and patience that I have been able to develop the academic and research abilities necessary to be successful in this field. Working with him has been an invaluable experience toward my professional development. I would like to thank the National Science Foundation for providing the financial support and the opportunity to conduct research in this complex field of study. I would also like to express my appreciation to Dr. Bassem Armaly as well as Dr. Ronald Kohser for serving on my committee and for their guidance through my academic career.

Second, I want to thank the staff of the Missouri S & T Mechanical Engineering Department for their support of my work in clerical, equipment, and fabrication assistance. I would also like to thank the following fellow Missouri S & T students who have provided indispensable help and assistance when needed throughout my graduate school experience – Jeff Massey, Brian Kaul, Nathan Wilke, and Jeff Wegener.

Finally, I would like to express my sincerest gratitude and appreciation to my wife, Jeanetta, for her unending love, support, and encouragement during the past seven years of my academic career, and also to my son Braden who provides the inspiration to present excellence, integrity, and value in everything I do.

TABLE OF CONTENTS

	Page
PUBLICATION THESIS OPTION	iii
ABSTRACT	iv
ACKNOWLEDGEMENTS	v
TABLE OF CONTENTS.....	vi
LIST OF ILLUSTRATIONS	ix
LIST OF TABLES	xii
NOMENCLATURE	xiii
 SECTION	
1. INTRODUCTION	1
2. LITERATURE REVIEW	3
2.1 Separation Criterion for Shear-driven Films in Separated Flows	3
2.2 Film Thickness Measurement Techniques for Dynamic Shear-driven Thin Liquid Films with Surface Instabilities	7
 PAPER	
1. <i>A Separation Criterion with Experimental Validation for Shear-driven Films in Separated Flows</i>	11
1. Introduction.....	12
2. Background.....	13
3. Scope	15
4. Experimental Facility	16
4.1 Shear-driven Film Test Section.....	16
4.2 High Speed Imaging System.....	18
4.3 Film Separation Measurement.....	18

5. Shear-Driven Film, Rough Wall Model	19
5.1 Gas Flow Model	20
5.2 Film Flow Model.....	23
5.3 Model Validation and Results	24
6. Separation Prediction by Analytical Force Balance.....	25
7. Experimental Results.....	29
7.1 Validation of Film Separation Criterion	29
7.2 Prediction of Wall Angle Effects	32
8. Summary and Conclusions	32
Acknowledgements.....	33
List of Figure Captions.....	34
Nomenclature.....	41
References	43
2. <i>Measurement of the Mean Film Thickness of Dynamic Shear-driven Thin Liquid Films using Optical Interferometry.....</i>	<i>45</i>
1. Introduction.....	46
2. Background.....	46
3. Theory of Technique	48
4. Experimental Facility	49
4.1 Shear-driven Film Test Section.....	49
4.2 Optical Hardware Configuration	51
4.2.1 Transmitting Optics.....	51
4.2.2 Receiving Optics	53
5. Image Analysis and Frequency Determination.....	55

5.1	Objectives and Key Ideas.....	55
5.2	Image Identification and Analysis Protocol.....	57
5.3	Image Processing Algorithm.....	58
5.3.1	Identification of Images with Fringes.....	58
5.3.2	Film Thickness Determination from Fringe Spacing	59
5.4	System Dynamic Range	60
6.	System Validation	62
7.	Experimental Results.....	62
8.	Summary and Conclusions	64
	Acknowledgements.....	64
	List of Figure Captions.....	65
	Nomenclature.....	75
	References	76
 SECTION		
3.	CONCLUSIONS.....	78
 APPENDICES		
A.	Experimental Setup - Test Section and Measurement Systems.....	80
B.	Film Separation Analysis Data Collection Procedure.....	85
C.	Film Thickness Measurement Data Reduction Procedure	88
D.	Film Thickness Measurement Technique - Laser Orientation Testing	99
E.	Improvements to the Interferometric Film Thickness Measurement Technique	104
	BIBLIOGRAPHY	107
	VITA.....	110

LIST OF ILLUSTRATIONS

PAPER 1

Figure 1.	Schematic of shear driven film interaction with separated gas phase flow resulting in partial film separation from the substrate at the corner.....	35
Figure 2.	Schematic of test section.	35
Figure 3.	Film width near the test section corner as a function of film flow rate and gas phase velocity.	35
Figure 4.	High speed imaging (2000 frames per second) of the film interaction with the separated gas flow at the test section corner.	36
Figure 5.	Picture of test section showing porous surface where film which remains attached after the corner is removed.	36
Figure 6.	Comparison of the results of the rough wall model used in this work and the experimental results reported in Wittig et al. [10].	36
Figure 7.	Typical results from the rough wall model used to predict film characteristics before the corner in the test section.....	37
Figure 8.	Momentum analysis for a control volume.	37
Figure 9.	Dimensionless gravitational term from Equation 21 as a function of Re_f	38
Figure 10.	Film Weber number as a function of Re_f	38
Figure 11.	Dimensionless Force Ratio as a function of Re_f	39
Figure 12.	Experimentally measured film separation by mass correlated to the calculated Force Ratio for various gas phase and liquid phase flow conditions. Surface tension is shown in parenthesis.	39
Figure 13.	Predicted effects of wall angle of the onset of film separation for various gas phase and liquid phase flow conditions.	40

PAPER 2

Figure 1. Schematic of the reflection of light off of the top and bottom surfaces of a film.	66
Figure 2. Schematic of experimental test section.	66
Figure 3. Schematic of the optical system for the interferometric film thickness measurement.	66
Figure 4. High-speed imaging of film flow showing Kelvin-Helmholtz instabilities on the surface of the film.	67
Figure 5. Schematic illustrating how curvature on the film surface affects the light rays exiting the film.	67
Figure 6. Comparison of image using frosted glass versus neutral density filter for the image target.	67
Figure 7. Image of film droplet used for interferometric film thickness measurement validation.	68
Figure 8. Droplet profile measurements used to calculate droplet volume.	68
Figure 9. Comparison of images for a) suspended sapphire disk, b) background noise,	69
Figure 10. Block diagram of image identification and analysis protocol.	69
Figure 11. FFT results from one high-speed image containing a discernable fringe pattern.	70
Figure 12. Histogram of dominant frequency/film thickness values for one image.	70
Figure 13. Distribution of film thickness values for flow conditions of 20m/s gas phase velocity and 13.01 cm ³ /s liquid flow rate comparing FFT and manual processing methods.	71
Figure 14. Results of FFT showing the low-end noise spike near zero.	71
Figure 15. Time series of thickness measurement results for 30 m/s gas phase velocity and 13.01 cm ³ /s liquid flow rate.	72
Figure 16. Distribution of film thickness measurements for three tests at 30 m/s gas velocity and 13.01 cm ³ /s liquid flow rate.	73
Figure 17. Distribution of film thickness measurements for tests at 30 m/s gas velocity and 6.46, 13.01, and 16.34 cm ³ /s liquid flow rates respectively.	74

APPENDICES

Figure 1. Schematic of experimental test section.	84
Figure 2. Schematic of the optical system for the interferometric film thickness measurement.	84
Figure 3. Picture of test section showing porous surface where film which remains attached after the corner is removed.	87
Figure 4. Block diagram of image identification and analysis protocol.	98

LIST OF TABLES

Table 1.	30 Degree Orientation Test Matrix and Results	103
Table 2.	45 Degree Orientation Test Matrix and Results	103

NOMENCLATURE

Symbol Description

A	area
CS	control surface
F_c	surface tension force at bottom of film
F_{ex}	external force
Fr_{hf}	film Froude number
F_s	surface tension force at top of film
g	gravitational constant
h_f	film thickness
k	turbulent kinetic energy
k_s	wall roughness
L_b	characteristic length of the film after the corner
\bar{n}	normal vector
Re_f	film Reynolds number
Re_{ks}	roughness Reynolds number
S_ϕ	source term
U_g	gas phase velocity
\bar{u}_{in}	initial fluid velocity vector
u_f	film velocity
u_{fs}	film surface velocity
u	fluid velocity component
v	fluid velocity component
\bar{v}	velocity vector
\dot{V}_f	film volumetric flow rate
W	gravitational force
We_f	film Weber number
We_{rel}	relative Weber number
w_f	film width

β	separated film angle from the horizontal
Γ_ϕ	effective diffusion coefficient
ε	dissipation
θ	surface corner angle from the horizontal
κ'	von Karman constant
μ_f	film viscosity
ρ_f	film density
σ	surface tension
τ	shear stress
ϕ	corresponding variable
ψ_τ	efficiency factor of film roughness
∇	gradient
∇	volume
F	number of fringes in the interference pattern
t	film thickness
n_g	index of refraction of gas
n_l	index of refraction of liquid film
β	angle of refraction (measured from the normal to the film)
δ	phase difference of the light reflected off of the top and bottom surfaces of the film
λ_0	wavelength of incident light
θ_i	incidence angle
m/s	meters per second
mm	millimeter
μm	micrometer
cm^3/s	cubic centimeters per second

Subscripts

p	first grid point
w	wall

1. INTRODUCTION

The dynamics of thin liquid films that develop on a solid surface and are driven by an adjacent gas flow have applications in many engineering problems, including fuel systems in internal combustion engines, liquid atomizer systems, refrigerant flows in evaporators, and film drag over wetted surfaces, and as such have been studied extensively. However, the dynamics of the film separation from the solid surface due to a sudden expansion in geometry, and its atomization by the separated/reattached gas shear layer, have received little attention. The films that are considered in this study can be classified as thin ($\sim 100 \mu\text{m}$), shear driven, and interacting with the adjacent separated gas flow.

In a port-fuel-injection engine, the liquid fuel accumulates as a film on the surfaces of intake valves and port walls during the cold-start period and enters into the cylinder by the shearing force of the intake air flow. It has been shown in numerous works (such as Felton et al. (1) and Dawson and Hochgreb (2)) that the liquid fuel usually deposits as thin films on the intake valve and port surfaces during the engine cold start period, and these films are seen to atomize to varying degrees with the inflowing air and enter the cylinder as droplets and ligaments. The presence of these films has been correlated to uHC emissions (Landsberg et al. (3), Stanglmaier et al. (4) among others). Knowledge of the characteristics of fuel film separation at sharp valve and port edges is essential to accurately predict the fuel/air mixture preparation for improved fuel efficiency and reduced emissions. To model these processes, a clearer understanding must be developed of the dynamics between the coupled gas phase (separated/reattached flow) and liquid phase, along with the details of the dominant interfacial instabilities. Of

particular interest in this study is the prediction of film separation from the solid surface as a function of gas phase velocity, liquid film flow rate, and wall angle.

Key to the development and validation of useful engineering models to simulate these flows is the measurement of the average film thickness on surfaces similar to those in each application. However, the characteristics of the solid substrate surface as well as the instabilities on the surface of the shear-driven film present significant challenges to techniques used to measure the film thickness. The nature of the shear-driven flow causes Kelvin-Helmholtz instabilities to exist on the top surface of the film. These instabilities cause the film thickness as well as the angle of the film surface to be constantly changing, making it very difficult to obtain a non-intrusive film thickness measurement. Also, measuring the film thickness on a variety of substrate surfaces limits the number of techniques available because access to the film is limited. Therefore, the lack of a reliable, inexpensive, non-intrusive technique to capture the mean thickness of shear-driven films on a variety of substrate surfaces motivates the current work.

2. LITERATURE REVIEW

Two distinct, yet intimately related, areas of research are presented in this thesis in two separate journal papers, and as such require separate reviews of the literature for background and previous work in the field. Therefore, the following literature review will be broken into two parts.

2.1. Separation Criterion for Shear-driven Films in Separated Flows

Two-phase flows have application in a multitude of engineering problems and as such have been studied by many investigators. The first part of this section of the literature review is intended to classify the problem at hand, given this vast range of applications for two-phase flows, in order to show a clear need for a separation criterion for shear-driven films in separated flows.

A significant amount of work can be found in the literature dealing with gas-liquid flows in pipes. The objective of these works is the prediction of transitions between the many propagation modes - stratified flow, annular flow, slug flows, and plug flows (5). Of these flow regimes, the films considered in the current study would be most similar to the annular flow condition, but with small film thickness scales.

Another related field is referred to as viscous thin film flow. The problem classification of these flows is determined by the force which drives the film. For example, the forces could include gravity (6), and moving pressure disturbances (7). The typical film thickness in the posed problem is on the order of 100 μm ; therefore, it would fit into this body of work. However, the driving force for this study is the shear force imparted by the adjacent gas flow, and therefore, the current problem is not classified into this flow regime.

As the film reaches the end of the supporting substrate and separates from the corner, breakup often occurs. A recent review of the literature concerning breakup processes of wall-bounded films, in comparison to jets and sheets, is given by Lightfoot (8). Some of the most comprehensive work done in shear-driven thin liquid films for atomization is that by Wittig and coworkers (9), (10), (11). Their work focused on prefilming atomizers for gas turbine engine applications, and in fact, some aspects of the liquid film transport model used to determine the input parameters for the proposed model are derived from the fine work of this group. Several important differences exist, however, between the geometry of a prefilming atomizer and the geometry considered here. For the prefilming atomizer, the shearing air is encountered on both sides of the thin liquid sheet once it departs from the atomizer. The solid substrate is effectively a splitter plate between the two air flows, coming to a sharp edge at the exit leaving no expanding wall corner to negotiate. Finally, gas phase velocities in the prefilming atomizer are on the order of 50 m/s (or much greater) to ensure significant atomization. As a result, the development of criteria to predict when the film separates is not applicable because the film always separates.

Three general theories have been proposed in the literature to predict film separation. The first, put forth by O'Rourke and Amsden (12), considers a balance between the inertia of the liquid film at a sharp corner in the wall and the pressure difference between the gas phase and the film at the wall. They argue that if the film inertia is small, a low pressure region forms on the wall side of the film, at the corner, and this causes the film to negotiate the corner and stay attached to the wall. However, if the inertia is large enough to cause the wall side pressure to drop to zero, then the film

will separate from the corner. It is also stated in their work that the surface tension effect is not included in their separation criterion because it can be shown to have negligible effect on the film separation, but no justification or experimental results are given to support omitting it. Shear stress and film thickness are shown to be major factors contributing to film separation according to the proposed model. However, no experimental validation of this model was performed.

The second approach is that of Maroteaux et al. (13), (14) who argued the film separation at a corner to be analogous to a Rayleigh-Taylor instability. In this approach, instabilities in the liquid film are amplified by a body force (i.e. normal acceleration) developed as the film rotates around the corner. The separation criterion is based on the ratio between the final and initial amplitude of the disturbance as the film flows over the edge. When the amplitude reaches a critical value, film separation from the edge occurs. Calibration of the model was done using a limited number of experiments to obtain a critical ratio of 20; however, several investigators have already commented on the validity of these results. Gubaidullin (15) points out several inconsistencies with the approach of Maroteaux et al. (13) including differences in the definition of the acceleration of the film at the corner. In addition, recent experimental work by Steinhaus et al. (16) suggest the analysis of Maroteaux et al. (13) shows different trends than what is observed experimentally.

The third approach, presented by Owen and Ryley (17), uses film inertia, surface tension, and body forces to estimate the radial stress of a film traveling around a rounded corner. The film is attached to the wall and has a specific radius and film thickness. Positive radial stresses represent compressive stresses which keep the film attached to the

wall, while negative stresses are tensile stresses which cause the film to separate from the wall. This approach is very similar to the criterion described in this thesis, in that the principle forces are the same, but several differences do exist between the two models and a closer look at the contributing forces reveals these differences. In the approach used by Owen and Ryley (17) the film that is separating from the wall is treated as a fluid particle. This assumption limits the ability of the model to capture the characteristics contributing to separation from both the gas and liquid flow conditions. In the current proposed approach, the liquid film separating from the wall is treated as a ligament, which involves both liquid and gas properties and velocities within a liquid Reynolds number and a relative Weber number. The liquid Reynolds number includes film velocity and film viscosity, while the relative Weber number includes the gas phase velocity, film velocity, and surface tension. None of these parameters are accounted for in the radial stress gravitational term used by Owen and Ryley (17), because the fluid is analyzed as a particle, not a separated ligament. Viewing the film as a ligament then, becomes quite significant due to the addition of many parameters in the gravitational and surface tension forces.

Neither the approach of O'Rourke and Amsden (12) or Maroteaux et al. (13), (14) have been rigorously compared to experiment, and both use rather ambiguous constants to fit the results to limited observations, which at times seem to be in conflict with the experimental observations of others. Also, the use of a characteristic ligament length to describe the film separating from the corner provides a better correlation than previous force balance methods over a wide range of experimental test conditions. Therefore, the proposed hypothesis outlined in this thesis considers the role of film inertia to overcome

surface tension and gravitational effects at the corner by representing the separating film as a characteristic liquid ligament in order to predict the onset of film separation.

2.2. Film Thickness Measurement Techniques for Dynamic Shear-driven Thin Liquid Films with Surface Instabilities

Thin film thickness measurements have been made using a wide variety of techniques. Klausner et al. (18) developed a technique for use with water, which uses capacitance sensors to measure the capacitance across the film to determine the film thickness. A crude model, developed by Chun et al. (19), was used to predict the capacitance as a function of film thickness. Experiments were conducted to measure film thicknesses ranging from two to twenty millimeters. The results obtained using the capacitance probes were compared to results obtained simultaneously using a CCD camera focused on the test section, with an average error of $\pm 2\%$ of full scale. The ability of this technique to capture accurate film thickness values below two millimeters is questionable. A similar method involving conduction probes was used by Suyari and Lefebvre (20). The probes are configured in a similar fashion, but instead use the conductance across the fluid to determine the film thickness. Both of these methods are intrusive and require accurate, high-resolution equipment to obtain a reliable result, making these techniques ill suited for this study.

Another class of non-intrusive techniques includes those that incorporate a laser light source. Laser-induced fluorescence, used by Schagen and Modigell (21), Maroteaux et al. (14), Yang and Melton (22), Driscoll et al. (23), Shaw II et al. (24), and Ting (25), requires one access point and uses either the fluorescent components in the liquid or an added dopant as the source of fluorescence. Images are captured using a

CCD camera and light intensities in each image are analyzed to determine the film thickness. Laser light absorption uses a similar approach, but uses light absorption instead of fluorescence and also requires two optical access points, usually above and below the film. (Mouza et al. (26), Barter et al. (27), (28), Wittig et al. (10)).

Another technique makes use of the total internal light reflection which occurs at a liquid-vapor interface because of the refractive index difference between the liquid and vapor (Hurlburt and Newell (29), Shedd and Newell (30)). The distance between the light source, which is perpendicular to the film, and the reflected light rays is proportional to the film thickness. Therefore, high-speed images are also captured for this technique and analyzed to determine the film thickness. This technique requires only one access point, but it must be below the film. Having an access point below the film greatly restricts the surface materials that can be used and hinders the use of these laser based techniques for many engineering applications.

Other methods used to determine film thickness include microwave absorption used by Roy et al. (31), and laser focus displacement used by Takamasa and Hazuku (32). All of these methods differ in ease of use, calibration, accuracy, cost and intrusiveness, and as such have advantages and disadvantages depending upon the application.

For the current application to shear-driven films with surface instabilities, the system must be able to obtain an accurate mean film thickness for a variety of substrate surfaces despite the film surface instabilities. Ideally this technique would require only one access point and would be suitable as a film thickness measurement technique for both wind tunnel and real application use, i.e. measurement of the film thickness on an intake valve or cylinder head. The interferometric approach is well suited for this type of

measurement because it is a non-intrusive point measurement, needs only one access point, requires minimal calibration, and is relatively inexpensive.

The interferometer approach was initially developed by Ohyama et al. (33), and makes use of the phase shift between the reflection of incident light from the top and bottom surfaces of the film. When the light approaches the film over a small range of incident angles, a portion of the incident light reflects at the top surface of the liquid film and a portion transmits through the film and reflects at the bottom surface. The refraction of light in the film causes the light exiting the film to interfere either constructively or destructively with the light reflected from the top surface, depending on whether the change causes the light waves to be in phase or out of phase. A calculation of the phase difference can be made based on the film thickness, wavelength of light, and indices of refraction of the liquid film and gas. For light that is incident over a range of angles, a series of light and dark fringes appear in the reflected light in the shape of concentric arcs. Therefore, combining the number of these fringes which occur in a specified field of view with the calculated phase difference, one can determine the film thickness at that instant. A set of experiments is shown by Ohyama et al. (33) which compares the interferometric thickness measurement with the average film thickness deduced from the volume and diameter of a lens of n-decane suspended on water. The two methods are in agreement, but there is no investigation of using this method for dynamic films.

Improvements were made to the interferometric technique by Nosoko et al. (34), who put forth an improved optical system in order to increase the accuracy and precision of the thickness measurement. This was achieved by using lenses with large f numbers and highly accurate focal lengths. The goal of this improvement was to minimize the

necessary calibrations to obtain an accurate film thickness. Experiments measuring the thickness of silicone oil films flowing down a vertical wall were performed, but no surface instabilities were present on these films, like in the currently proposed application. An attempt was also made to quantify the error in the measurement, which ranged from about one to ten percent depending on the angle of incidence used.

The most recent work using optical interferometry to measure film thickness was by Kelly-Zion et al. (35) who measured the transient thickness of an evaporating film. The motivation for this application was to measure the thickness of fuel that impinges on surfaces inside an internal combustion engine. The thickness of the films that were measured changed very quickly due to the evaporation, however, the angle of the top surface of these films was unchanging and remained parallel to the solid surface. This is quite different from the application of this technique to shear-driven films with surface instabilities, where the angle of the top surface is constantly changing. Kelly-Zion and coworkers (35) also developed an algorithm to count the number of fringes within the images. The images captured in their study contained fringes over the entire image in every image. When applying this approach to shear-driven films, however, this is not the case, and therefore the algorithm developed by Kelly-Zion et al. (35) could not be used when applying this technique to shear-driven films.

As the published literature does not indicate any temporally and spatially resolved thickness measurements of shear-driven films with surface instabilities made using this method, the focus of this research is on the enhancement of the technique reported by Nosoko et al. (34) and Kelly-Zion et al. (35) by application of this technique to measure the average thickness of dynamic shear-driven films with surface instabilities.

PAPER 1**A Separation Criterion with Experimental Validation for Shear-driven
Films in Separated Flows****M.A. Friedrich, H. Lan, J. L. Wegener, J.A. Drallmeier, and B.F. Armaly****Department of Mechanical and Aerospace Engineering****Missouri University of Science and Technology****400 West 13th Street****Rolla, MO 65409-0050 USA****Abstract**

The behavior of a shear-driven thin liquid film at a sharp expanding corner is of interest in many engineering applications. However, details of the interaction between inertial, surface tension, and gravitational forces at the corner that result in partial or complete separation of the film from the surface are not clear. A criterion is proposed to predict the onset of shear-driven film separation from the surface at an expanding corner. The criterion is validated with experimental measurements of the percent of film mass separated as well as comparisons to other observations from the literature. The results show that the proposed force ratio correlates well to the onset of film separation over a wide range of experimental test conditions. The correlation suggests the gas phase impacts the separation process only through its effect on the liquid film momentum.

1. Introduction

The dynamics of thin liquid films that develop on a solid surface and are driven by an adjacent gas flow have applications in many engineering problems, and as such have been studied extensively. The dynamics of the separation of such films from the solid surface due to a sudden expansion in geometry and its atomization by the separated/reattached gas shear layer (see Fig. 1), however, have received little attention. The films that are considered in this study can be classified as thin ($\sim 100 \mu\text{m}$), shear driven, and interacting with the adjacent separated gas flow. Such complex interaction between the liquid film and the gas in separated flow is encountered in fuel and air mixture preparation for spark ignition engines, as well as in atomizer design, refrigerant flows in evaporators, and wave plate mist eliminators.

For example, in a port-fuel-injection engine, the liquid fuel will normally accumulate as a film on the surfaces of intake valves and port walls during the cold-start period and enter into the cylinder by the shearing force of the intake air flow. It has been shown in many works (such as Felton et al. [1] and Dawson and Hochgreb [2]) that the liquid fuel usually deposits as thin films on the intake valve and port surfaces during the engine cold start period, and these films are seen to atomize to varying degrees with the inflowing air and enter the cylinder as droplets and ligaments. The presence of these films has been correlated to uHC emissions (Landsberg et al. [3], Stanglmaier et al. [4] among others). Knowledge of the fuel film separation at sharp valve and port edges is essential to accurately predict the fuel/air mixture preparation for improved fuel efficiency and reduced emissions. To model these processes, a clearer understanding must be developed of the dynamics between the coupled gas phase (separated/reattached

flow) and liquid phase, along with the details of the dominant interfacial instabilities. Of particular interest in this study is the prediction of film separation from the solid surface as a function of gas phase velocity, liquid film flow rate, and wall angle.

2. Background

Gas-liquid flows have application in a multitude of engineering problems and as a result have been studied for many years. An attempt is made here to classify the problem at hand, given this large body of research which is found in many fields.

A significant amount of work can be found in the literature dealing with gas-liquid flows in pipes. An often stated objective in this body of work is the prediction of transitions between the many propagation modes including stratified flow, annular flow, slug flows, and plug flows [5]. Of these flow regimes, the films considered in this problem would be most similar to the annular flow condition, but with small film thickness scales.

Another related field is referred to as viscous thin film flow. Here, the force which drives the film determines the problem classification. For example, driving forces could include gravity [6], and moving pressure disturbances [7]. Given that the typical film thickness in the posed problem is on the order of 100 μm , it would fit into this body of work. However, the driving force for this study is the shear force imparted by the adjacent gas flow phase.

Once the film reaches the end of the supporting substrate, breakup often occurs. A recent review of the literature concerning breakup processes of wall-bounded films, in comparison to jets and sheets, is given by Lightfoot [8]. Some of the most comprehensive work done in shear-driven thin liquid films for atomization is that by

Wittig and coworkers [9-11], where their work focused on prefilming atomizers for gas turbine engine applications. In fact, some aspects of the liquid film transport model used here are derived from the fine work of this group. Several important differences exist, however, between the geometry of a prefilming atomizer and the geometry considered here. For the prefilming atomizer, the shearing air is encountered on both sides of the thin liquid sheet once it departs from the atomizer. The solid substrate is effectively a splitter plate between the two air flows, coming to a sharp edge at the exit leaving no expanding wall corner to negotiate. Finally, gas phase velocities in a prefilming atomizer are on the order of 50 m/s (or much greater) to ensure significant atomization. As a result, the development of criteria to predict when the film separates is not applicable.

Two general theories have been proposed in the literature to predict film separation. The first, put forth by O'Rourke and Amsden [12], considers a balance between the inertia of the liquid film at a sharp corner in the wall and the pressure difference between the gas phase and the film at the wall. No experimental validation of this model was done. The second approach is that of Maroteaux et al. [13,14] who argued the separation at a corner to be analogous to a Rayleigh-Taylor instability. In this approach, instabilities in the liquid film are amplified by a body force (i.e. normal acceleration) developed as the film rotates around the corner. Calibration of the model was done using a limited number of experiments. However, Gubaidullin [15] points out several inconsistencies with the approach of Maroteaux et al. [13] including differences in the definition of the acceleration of the film at the corner. In addition, recent work by Steinhaus et al. [16] suggests the analysis of Maroteaux et al. [13] shows different trends than what is observed experimentally.

Neither the approach of O'Rourke and Amsden [12] or Maroteaux et al. [13, 14] have been rigorously compared to experiment and both use rather ambiguous constants to fit the results to limited observations, which at times seem to be in conflict with the experimental observations of others. Our hypothesis considers the role of film inertia to overcome surface tension and gravitational effects at the corner.

3. Scope

The key objective of this study is the analytical development and experimental validation of a comprehensive separation criterion for predicting the film behavior at the corner. The criterion must be able to capture whether the film will separate from the corner to break up into droplets or negotiate the corner and stay attached. To this end, the development of a test facility to create, control, and observe a shear-driven liquid film up to a sudden expansion (corner) is discussed. The criterion was formulated and developed to be a submodel of a larger numerical model used to predict film propagation along a surface. Hence, quantitative estimates of the film thickness and average film velocity just before separation are required as inputs to the separation criteria. For this study, these are obtained using a simple two-dimensional shear-driven film simulation model, based on the work of Wittig and coworkers [9-11]. This film simulation model was chosen based on its extensive use and validation presented in the literature. Clearly other simulation approaches could be used for this (e.g. a VOF type model as presented by Thiruvengadam et al. [17]). The focus of this study, then, is not the film propagation before the corner, but the development of a force balance model to predict the onset of film separation at the corner given these inputs of film thickness and average film velocity. Observations using high speed imaging of the film separation phenomena, as

well as quantitative measures of liquid film mass attached to the wall after the corner are used to discuss the effectiveness of the developed force balance model.

4. Experimental Facility

4.1 Shear-driven Film Test Section

The flow facility consists of a four part test section mounted to an optics table platform. Flow is pulled through the test section using a large liquid ring vacuum pump. Flow rates through the test section are determined using a laminar flow element. Corrections are made for local temperatures and pressures resulting in uncertainties of less than 3% in the flow rate.

A schematic of the test section is shown in Fig. 2. A 1.43 m long entrance region (not shown) provides for two-dimensional flow span-wise across the test section at the point of film introduction. The dimensions of the test section at the point of film introduction and up to the corner are 2 cm tall by 10 cm wide, giving an aspect ratio of 5. The liquid is introduced through a porous brass plug on the bottom wall in the film introduction section. Simulations indicate that with the entrance region previously specified, flow should be 2-dimensional with this aspect ratio (i.e. limited wall effects) for the center 7.5 cm of the test section. It is over this center 7.5 cm width of the test section that the film is introduced. The liquid flow into the test section is quantified on a volumetric flow basis and measured using a rotometer with an uncertainty of 2.5%. For the results presented here, the liquid was water with the addition of a surfactant (Surfynol 465) at 0.1% and 1.0% by mass which results in a surface tension, σ , of 0.042 N/m and 0.026 N/m, respectively. The surfactant had minimal effect on the fluid viscosity which

was measured to be $0.983 \times 10^{-3} \text{ Ns/m}^2$ for the 0.1% solution and $1.027 \times 10^{-3} \text{ Ns/m}^2$ for the 1.0% solution, effectively the same as water at ambient conditions.

The corner section is removable from the configuration such that the angle of the corner in the bottom wall may be changed. Currently a 60° angle, measured from the horizontal, is being used. The length of the duct from the point of film introduction to the corner is 23 cm. After the corner, the duct has an aspect ratio of 1.429 wherein an exit section provides for a transition from the test section to the 10.2 cm diameter piping which runs to the liquid ring pump. Great care is taken to ensure the test section is horizontal to prevent biasing of the film flow.

Significant effort was expended in developing a test section which resulted in uniform gas phase velocities span-wise across the test section near the corner. Although the film is introduced uniformly over the center 7.5 cm width of the test section, the film width changes as it reaches the corner due to surface tension. Figure 3 shows the typical variation in the width of the film, 5 mm from the corner, as a function of gas phase velocity for a surface tension of 0.042 N/m. The film width is measured based on imaging through a window in the top of the test section with an uncertainty of 3 % determined by parallax and scale resolution. Clearly increased gas velocity, and hence shear force, keeps the film spread over the test section lower wall, counteracting the surface tension forces. These same surface tension forces impact the film separation at the corner and will be discussed in the development of the separation criterion.

The liquid film flow condition is characterized by the use of a film Reynolds number, Re_f , based on the volumetric flow introduced to develop the film, \dot{V}_f , and the measured film width, w_f , at each flow condition:

$$Re_f = \frac{\dot{V}_f \rho_f}{w_f \mu_f} \quad (1)$$

Each flow condition can then be characterized by a gas phase velocity, U_g , and the film Reynolds number, Re_f . A range of experimental gas and liquid phase flow conditions were considered. Gas phase velocities ranged from 20 to 45 m/s and liquid flow rates varied from 6.5 to 41.5 cm³/s. This results in a variation of film Re_f from approximately 100 to 400.

4.2 High Speed Imaging System

The general characteristics of the liquid film, including the surface instabilities and interaction of the film with the separated gas phase at the corner, were characterized using high speed imaging. A Photron 1280 PCI high speed camera, with close-up lenses totaling +7 diopter, was used to capture 2000 frames per second at 640 X 256 resolution. A typical image from this system is shown in Fig. 4. The spatial resolution of these results is determined by the pixel resolution of the camera. At the current magnification, the spatial resolution shown in Fig. 4 is approximately 100 microns.

4.3 Film Separation Measurement

Measurement of the degree to which the liquid film is separated from the corner is made by pulling off the liquid which stays attached to the downward sloping wall after the corner. A porous brass plug was placed downstream of the test section corner on the downward slope of the lower wall as a means to extract the mass of the liquid film that stays attached to the wall. As shown in Fig. 5, the porous plug (6 mm wide) extends across the span of the test section and is flush with the sloping wall to prevent any disturbance of the flow. The brass plug is located 6 mm from the corner, which was

determined by flow visualization to be far enough from the corner as to not impact the film separation process and yet not low enough to capture liquid which may be pulled up the sloping wall by the recirculation flow region behind the step. Suction is applied below the porous plug to draw the liquid from the wall, which is then captured and the mass measured. Sufficient suction is applied behind the porous plug, adjusted at each flow condition, for complete removal of the liquid from the wall without pulling the gas through the porous surface. Imaging is used at each set point to ensure the liquid film was removed.

Film suction collection times were on the order of 1 minute in duration with an uncertainty of 1%. The captured volume is weighed to establish a mass flow of liquid attached to the wall, which, along with the measured liquid flow into the test section, provides the mass flow of liquid separated at the corner. Combined uncertainty in this measurement is 5 %.

5. Shear-Driven Film, Rough Wall Model

A CFD model is used to study the shear-driven liquid film propagation along the bottom wall of the test section. The focus of the current work is the development of a separation model for use in the context of a comprehensive numerical film model, hence the film propagation model, chosen from the literature, is used to predict film thickness and film velocity at the wall corner, before the point of separation. A brief description of the chosen model is given, followed by a few predictions of film characteristics.

The two-dimensional rough wall model proposed by Sattelmayer and Wittig [9] for simulating shear-driven liquid film flow is used. This model has been shown to provide good agreement with measured values for the average film thickness [10, 11].

The model treats the liquid film as an equivalent rough wall interacting with the turbulent gas flow, with the wall roughness being a function of the interfacial shear stress and the average film thickness. The interfacial shear stress provides the coupling between the liquid and the gas flows, and an iterative procedure is developed to arrive at a converged solution. This scheme was implemented in a computational code to numerically simulate the development of the shear-driven liquid film in the turbulent gas flow inside the experimental duct geometry.

5.1 Gas Flow Model

The two-dimensional incompressible Reynolds-averaged Navier-Stokes equations, along with the continuity equation, were used to simulate the gas flow. The $k - \varepsilon$ turbulence model was utilized with wall functions (high-Reynolds-number model) applied to the rough wall (the film boundary), and low-Reynolds-number model applied to the other smooth wall of the duct. The general form for the governing equations can be represented by:

$$\frac{\partial u}{\partial x} + \frac{\partial v}{\partial y} = 0 \quad (2)$$

$$\nabla \cdot (\rho \phi \bar{V}) = \nabla (\Gamma_{\phi} \nabla \phi) + S_{\phi} \quad (3)$$

where, Γ_{ϕ} is an effective diffusion coefficient and S_{ϕ} denotes the source term [19]. The governing equations for the two velocity components (u , and v), the turbulent kinetic energy (k), and its dissipation (ε) can be represented by Eq. 3, where ϕ is the corresponding variable and \bar{V} is the velocity vector. These equations were discretized using a finite volume method in a staggered grid system, with the SIMPLE algorithm used to deal with the coupling between flow and pressure grids. The discretized equations

were solved by a line-by-line TDMA (Tri-Diagonal Matrix Algorithm) method. Several grid densities and distributions (non-uniform) were considered to insure a grid independent solution, and a grid of 120(X) and 66(Y) was selected for generating the final results. The use of higher grid densities (i.e. 1.5 and 2 times greater than the one cited above) had minimal effect on the final results. The approximate relative error in film thickness is 1.9% and in film velocity is 2.2% when the grid is doubled. At least 5 grid points were set inside the laminar sublayer near the smooth wall where the low-Reynolds-number turbulence model was used; on the other hand, the first grid point for the gas flow near the rough wall (liquid film) is placed outside of viscous sublayer where $11.3 \leq y_p^+ \leq 40$ is satisfied. The grid for simulating the turbulent gas flow is distributed between the first grid point “ p ” near the rough wall and the smooth wall.

The wall roughness (or liquid film) effect, k_s , is incorporated into the logarithmic law of the rough wall through the following relations:

$$u_p^+ = \frac{1}{\kappa'} \ln y_p^+ + C(\text{Re}_{k_s}) \quad (4)$$

where, $u_p^+ = \frac{u_p (c_\mu^{1/4} k_p^{1/2})}{\tau_p / \rho}$, $y_p^+ = \frac{y_p (c_\mu^{1/4} k_p^{1/2})}{\nu}$, and $C(\text{Re}_{k_s})$ is a function that is dependent on the

roughness Reynolds number, $\text{Re}_{k_s} = \frac{(c_\mu^{1/4} k^{1/2}) k_s}{\nu}$. The functional relation for $C(\text{Re}_{k_s})$ can be

found in the literature [10]. The term y_p is the distance of the first grid point in the computational domain for the gas flow from the rough wall. The shear stress τ_p is given by [19]:

$$\tau_p = \frac{\rho c_\mu k_p^2 u_p}{y_p \varepsilon_p} \quad (5)$$

To start the gas flow simulations, initial values for all of the dependent variables need to be assumed as $u = \bar{u}_{in}$, $v = 0$, $k = 0.005\bar{u}_{in}^2$, $\varepsilon = 0.1k^2$. In addition, for a given liquid film volume flow rate (\dot{V}_f / w_f), the average film thickness (h_f) needs to be assumed at the start of the simulation. This provides a means for calculating the average film velocity and the wall shear stress from the following relations:

$$h_f \bar{u}_f = \dot{V}_f / w_f, \text{ and } \tau_w = 2\mu_f \frac{\bar{u}_f}{h_f} \quad (6)$$

Note that the velocity distribution of shear-driven liquid film is assumed to be linear (i.e. $u_{fs} = 2\bar{u}_f$ where u_{fs} is the film surface velocity). The wall roughness is evaluated by using the following relations [18]:

$$k_s = \psi_\tau \cdot h_f \quad (7)$$

$$\psi_\tau = 1.47 + 0.01851 \tau_w \quad (8)$$

The boundary conditions for the low-Reynolds-number turbulent model that are used on the smooth wall of the duct are $u = v = k = 0$, $\varepsilon = 2\nu k_p / y_p^2$ at the wall. In the high-Reynolds-number turbulent model, the boundary conditions that are applied at y_p consisted of u_p that is computed from the logarithmic law of the wall (Eq. 4), and

$$\varepsilon_p = \frac{c_\mu^{3/4} k_p^{3/2}}{\kappa y_p}, \text{ while the boundary conditions for } v \text{ and } k \text{ are applied at the wall as } \frac{\partial v}{\partial y} = 0,$$

$\frac{\partial k}{\partial y} = 0$. The inlet velocity distribution of the gas flow was equivalent to fully developed turbulent flow and the exit conditions were taken as fully developed. The shear stress at “p”, which is considered to be constant between “p” and the rough wall, is evaluated using Eq. 5 and the simulated gas flow results.

5.2 Film Flow Model

The liquid film flow is simulated by using the laminar boundary layer flow approximation that is governed by the following simplified Navier-Stokes equation:

$$\rho_f (u_f \frac{\partial u_f}{\partial x} + v \frac{\partial u_f}{\partial y}) = \frac{\partial \tau}{\partial y} \quad (9)$$

Assuming a linear velocity distribution through the film, and using the integral method (i.e. integrating the above momentum equation together with continuity equation (Eq. 2) in the y direction from 0 to $h(x)$), yields the following ordinary differential equation for the surface film velocity:

$$\frac{du_{fs}(x)}{dx} = \frac{3}{2\rho_f \dot{V}_f} (\tau_p - \tau_w) \quad (10)$$

where τ_p is evaluated from Eq. 5, and τ_w is evaluated from Eq. 6. A fourth-order Runge-Kutta integration scheme with adaptive step-size control is used to determine the local surface film velocity from Eq. 10, and from these results the local film thickness is evaluated and used to evaluate the average film thickness over the length of the calculation domain. The resulting average film thickness is used to update the effective wall roughness, and this new wall roughness is used to start a new gas flow simulation. This iterative procedure is repeated until the difference between the evaluated shear stress at the first grid point “ p ” for two iterations, $(\tau_p^n - \tau_p^{n+1})$, is smaller than 10^{-6} . At that state τ_p becomes equal to τ_w for most of the simulated domain downstream except for the injection region of the liquid film. A starting film thickness is needed to initiate the computation of the film flow, and that film thickness is updated after every iteration during the coupling iteration process.

5.3 Model Validation and Results

To verify our numerical simulation code using the rough wall model, a reproduction of the experiment described in Wittig et al. [10] was performed. The experimental configuration was similar to the one used in this study in that a shear driven film was established on a plate. However, the gap height between the bottom plate and the top plate of the test section was only 0.4 cm, compared to 2 cm for this work. As expected, the rough wall model developed for this work produced results quite similar to those reported by Wittig et al. [10] and matched well to their reported experimental measurements, as shown by the film thickness and surface velocity data shown in Fig. 6. Note that this was not a validation of the shear-driven film model of Sattelmayer and Wittig [9], which has been performed and presented in the literature [10,11], but instead was a verification of the simulation code used to obtain the film thickness and average film velocity as inputs for the developed force balance model.

Finally, Fig. 7 shows typical results of the simulations for the test section and fluid described under *Experimental Facility*. The simulations were performed for the film introduction section and the corner section up to, but not including the corner. The purpose of the simulations was to provide reasonable estimates for the average film velocity and the average film thickness at the corner, for input into the film separation criteria. The simulation results show that for a fixed inlet air velocity the liquid film thickness and its velocity increase as the liquid flow rate (or Re_f) increases for this two-dimensional simulation. On the other hand for a fixed liquid flow rate (Re_f), the liquid film thickness decreases but its average velocity increases as the inlet air velocity increases.

6. Separation Prediction by Analytical Force Balance

When the liquid film flow reaches the sharp corner, the bulk of the liquid may separate from the wall and then breakup into droplets by the aerodynamic force of the gas, or turn the corner and remain attached to the inclined wall, depending on the flow conditions of both the gas and liquid phase. To determine the behavior of the bulk film at the corner, an appropriate separation criterion needs to be established. For the analysis here, the forces considered are film inertia, surface tension, and body forces.

To consider this balance of forces at the corner, an approach similar to that of Hartley [20], Hartley and Murgatroyd [21], and Penn et al. [22] for the analysis of dry patches on flat surfaces is used. A 2-dimensional control volume is drawn around the liquid film, in this case at the point of separation, and a linear momentum conservation law is written for the control volume.

As shown in Fig. 8, a control volume, represented by dashed lines, is chosen perpendicular to the film flow at the corner and surrounding the presumed separated film after the corner at an angle of β from the horizontal. The surface expands at an angle θ with the horizontal. The force balance is made perpendicular to the film, in the p -direction, to ascertain the equilibrium position of the separated film by balancing the perpendicular forces on the film. External forces considered are the surface tension force at the top of the film, F_s , the surface tension force at the bottom of the film, F_c , as well as a gravitational force, W . The surface tension force at the bottom of the film, F_c , is presumed to act perpendicular to the control surface, in the negative p -direction, at the meniscus between the separated liquid and the film that remains on the wall.

When the film approaches the corner, the effect of its momentum is to drive the film to separate from the corner which is balanced by the two surface tension forces as well as the gravitational force. This balance is established by considering conservation of linear momentum for steady conditions for the p-direction. Beginning with

$$\iint_{cs} \rho_f u_f (\vec{V} \cdot \vec{n}) dA = \rho_f \vec{g} \cdot \vec{V} + \vec{F}_{ex} \quad (11)$$

the momentum flux entering the control volume in the p-direction, assuming uniform flow at the mean film velocity, u_f , is given by

$$-\rho_f \dot{V}_f u_f \sin \beta. \quad (12)$$

There is no momentum flux in the p-direction exiting the control volume. For the external forces, F_{ex} , acting on the control volume, the surface tension force on the upper surface, F_s , is

$$-\sigma w_f \sin \beta \quad (13)$$

while for the lower surface, the surface tension force, F_c , acts in the negative p-direction and is given by

$$-\sigma w_f. \quad (14)$$

To consider the magnitude of the gravitational force, a characteristic length of the film after the corner, L_b , must be established. Using the experimental correlations of Arai and Hashimoto [23] for thin sheet breakup, a characteristic breakup length is given by

$$L_b = 0.0388 h_f^{0.5} Re_f^{0.6} We_{rel}^{-0.5}. \quad (15)$$

For this correlation, the Reynolds number of the film is defined as

$$Re_f = \frac{h_f u_f \rho_f}{\mu_f} \quad (16)$$

and the Weber number is based on the relative velocity between the gas phase and the liquid film

$$We_{rel} = \frac{h_f \rho (U_g - u_f)^2}{2\sigma} \quad (17)$$

where ρ is the gas phase density. Given that the film volumetric flow is

$$\dot{V}_f = u_f w_f h_f, \quad (18)$$

and combining the external forces, the p-direction linear momentum balance, per unit width, results in

$$\rho_f u_f^2 h_f \sin \beta = \sigma \sin \beta + \sigma + \rho_f g h_f L_b \cos \beta. \quad (19)$$

The above relation provides a means by which the film angle, β , can be determined which balances the film momentum flux with the external forces of surface tension and weight. This “equilibrium” film angle should provide a measure, when compared to the corner angle, θ , of whether the bulk of the liquid film will separate. However, measuring this “equilibrium” film angle is very difficult experimentally due to the characteristic unsteadiness in the flow.

If film separation is considered to exist for any β less than θ , then a critical force ratio can be obtained by setting $\beta = \theta$. Doing so in Eq. 19 and normalizing by the surface tension, one finds the following ratio of the inertial force to the surface tension and gravitational forces:

$$Force\ Ratio = \left\{ \frac{\rho_f u_f^2 h_f \sin \theta}{\sigma \sin \theta + \sigma + \rho_f g h_f L_b \cos \theta} \right\} \quad (20)$$

or nondimensionalizing gives

$$Force\ Ratio = \left\{ \frac{We_f}{1 + \frac{1}{\sin \theta} + Fr_{h_f} We_f \left(\frac{L_b}{h_f} \right) \left(\frac{1}{\tan \theta} \right)} \right\} \quad (21)$$

where $We_f = \frac{\rho_f u_f^2 h_f}{\sigma}$, $Fr_{h_f} = \frac{gh_f}{u_f^2}$ and $Re_f = \frac{\rho u_f h_f}{\mu}$. This force balance is effectively a

Weber number modified by the wall angle due to the surface tension at the lower surface and a gravitational force effect. This differs from previous Weber number models [24] in the inclusion of the effects of the wall angle as well as body forces on the separation process. It differs from the force analysis of Owen and Ryley [25] by the inclusion of additional surface tension forces which provide the wall angle dependence seen experimentally. Arguably, when the Force Ratio becomes greater than one, the inertial force becomes great enough for the film to begin to separate from the wall. Hence, a Force Ratio of one can be used as a criterion for the onset of film separation. Clearly, since the unsteady nature of the film surface has not been considered, as displayed in Fig. 4, one could not expect all of the liquid film to separate at this point. If however, the appropriate forces have been captured, for Force Ratios greater than one some measurable film mass should be separated since sufficient film inertia exists, whereas below one all the film mass should remain attached to the wall.

The various dimensionless terms in Eq. 21 can be calculated knowing the film thickness and velocity along with the fluid properties. To observe the general behavior of the various force terms, the film velocity and thickness are calculated using the rough wall model, for example as shown in Fig. 7. With these predictions, Fig. 9 shows the variation of the dimensionless gravitational force term

$$Fr_h, We_f \left(\frac{L_b}{h_f} \right) \left(\frac{1}{\tan \theta} \right) \quad (22)$$

in the denominator of Eq. 21 as a function of Re_f . Clearly, the gravitational effect becomes more significant at higher Re_f , which from Fig. 7 corresponds to thicker films. The film We_f , shown in Fig. 10, captures the force balance between the surface tension and the film inertia at the corner. As expected, the We_f increases with Re_f due to the increase in film inertia.

Finally, the Force Ratio defined in Eq. 21 is shown as a function of the Re_f for various gas phase velocities in Fig. 11. The rather significant difference in the Force Ratio for different gas phase velocities at higher Re_f seems to be driven by the gravitational term, as shown in Fig. 9 which becomes significant at these higher Re_f . If the above force balance is capturing the appropriate physics, then the film should begin to separate from the wall when the Force Ratio in Eq. 21 becomes greater than one. Figure 11 suggests, then, that films with lower Re_f would be more likely to stay attached to the wall. Similarly, films driven by lower gas phase velocities would also tend to stay attached. Based on Figs. 7 and 11, films would need to be quite thick at lower gas phase velocities (leading to higher relative film velocities) to begin to separate from the wall. To test the viability of the above force balance to predict the onset of film separation, film separation experiments were conducted.

7. Experimental Results

7.1 Validation of Film Separation Criterion

Film separation experiments were made for gas phase velocities between 20 and 45 m/s and Re_f between 100 and 400. Validation of the separation criterion was

performed by measuring the percent of liquid mass that remained attached to the wall after the corner. For each experimentally determined gas phase velocity and Re_f , as established by the liquid flow rate and film width, the rough wall model was used to predict the film velocity, u_f , and film thickness, h_f . This provided sufficient information for calculating the Force Ratio, as per Eq. 21.

Results for 68 different flow conditions are shown in Fig. 12. For each gas phase velocity, several liquid film flow rates were established; with the film width and liquid mass attached to the wall measured for each set point. Two water-surfactant mixtures were used to study the effect of surface tension. Two important features should be noted from these results. First, the Force Ratio appears to reduce the results from a wide range of experimental conditions into a common trend. The results varied from cases where no liquid was separated from the wall (i.e. the film remained attached) to approximately 90 % of the liquid mass separated from the wall near the corner. The second important observation is that the Force Balance performed for this analysis appears to capture quite well the onset of the film separation process. For the range of conditions examined, the start of the film separation process begins when the inertial film force is greater than the restoring forces, i.e. at a Force Ratio of one. As the Force Ratio increases from one, a continual increase in the mass of the film separated from the corner was observed. A determination of when the film is “separated” versus “not separated” is not made here as this determination is a bit arbitrary. In fact the results show that under many flow conditions a “partial separation” occurs where a fraction of the liquid mass separates with the remainder staying attached to the wall. However, as can be seen in Fig. 12, the Force Ratio model predicts quite well the onset of film separation from the corner at a force

ratio of near one, with approximately 50% of the liquid mass separating at a force ratio of two for most flow conditions.

The ability of a force balance at the corner to capture the onset of the film separation process suggests that the appropriate forces are being included, at least over the range of flow conditions studied. This suggests that the model established by O'Rourke et al. [12] is inconsistent with this work in that it argues the importance of the gas phase pressure on either side of the film and does not include surface tension effects. Clearly, the nature of the gas phase shear, particularly the shear layer and recirculation zones as depicted in Fig. 1, will impact the breakup process. However, the separation process only appears to be affected by the gas phase field through the film inertia, established by the shear driven boundary condition.

Although the flow conditions and fluid properties were quite different than those considered in this study, a few comments can be made in regard to the force balance developed here and the experimental observations of Steinhaus et al. [16]. Steinhaus et al. [16] observed that higher film flow rates (i.e. Re_f) generally resulted in more film separation, which agrees with the trends shown in Fig. 11. However, they commented that the film flow rate seemed to have a relatively small effect. This may be due to the fact that their study considered only very high gas phase velocities (between roughly 70 and 200 m/s) which resulted in very thin films (less than 100 microns) for the liquid considered. With Re_f all well less than 100 in their experiments, the decreasing slope shown in the Force Ratio at low Re_f in Fig. 11 would suggest a lessening dependence on Re_f . Steinhaus et al. [16] also noted that very high gas phase velocities (greater than 200 m/s) were necessary to “preferentially strip” the liquid film for low liquid flow rates (Re_f

< 10) for a 45° wall angle. Again, this observation fits well with the trend shown in the Force Ratio of Fig. 11, which suggests gas phase velocities would need to far exceed the 45 m/s considered here for the onset of separation (Force Ratio = 1) at a wall angle of 60°.

7.2 Prediction of Wall Angle Effects

It is important to note that the ability of the Force Ratio to capture the onset of film separation leads to a predictive capability. For example, using the rough wall film model, the Force Ratio can be calculated for a given set of gas phase velocity, liquid flow rate and wall angle. Considering those conditions which provide a unity Force Ratio for a chosen wall angle, prediction of the onset of film separation can be established, as shown in Fig. 13. As indicated on the figure, to the right of the curves are flow conditions which result in a Force Ratio larger than one for the given wall angle and would suggest the occurrence of some degree of film separation; to the left of the curves are Force Ratios less than one which would imply no separation. The results suggest that the wall angle has a lesser effect on film separation for steeper wall angles. Additionally, the impact of wall angle on the separation process is more significant for lower gas phase velocities and of lesser importance for higher gas phase velocities.

8. Summary and Conclusions

An experimental test facility to study the development of a shear-driven liquid film and its subsequent separation at an expanding corner has been developed. Built into the test section is the ability to measure the liquid mass which stays attached to the wall after the corner. An analytical force balance was developed to serve in a predictive sense as a criterion for the onset of film separation. Required for the force balance is

knowledge of the film thickness and velocity at the corner, which for this study, were determined using a simple rough wall film propagation model.

The force balance of the major liquid phase forces acting at the corner, including surface tension, film inertia, and gravity, correlated well to the onset of film separation as measured in the experiment. Unlike previous Weber number models, effects of the wall angle on film separation are included. Additionally, the mass fraction of the liquid film which separates from the wall correlates to the Force Ratio over a wide range of experimental test conditions. The correlation of the separated mass to the liquid film force balance suggests the gas phase impacts the separation process only through its effect on the liquid film momentum. It is surmised, however, the inclusion of gas phase effects in the shear layer and recirculation zone will be necessary to consider the breakup of the film.

Acknowledgements

This work was supported in part by NSF grant CTS-0352135.

List of Figure Captions

- Figure 1. Schematic of shear driven film interaction with separated gas phase flow resulting in partial film separation from the substrate at the corner.
- Figure 2. Schematic of test section.
- Figure 3. Film width near the test section corner as a function of film flow rate and gas phase velocity.
- Figure 4. High speed imaging (2000 frames per second) of the film interaction with the separated gas flow at the test section corner.
- Figure 5. Picture of test section showing porous surface where film which remains attached after the corner is removed.
- Figure 6. Comparison of the results of the rough wall model used in this work and the experimental results reported in Wittig et al. [10].
- Figure 7. Typical results from the rough wall model used to predict film characteristics before the corner in the test section.
- Figure 8. Momentum analysis for a control volume.
- Figure 9. Dimensionless gravitational term from Equation 21 as a function of Re_f .
- Figure 10. Film Weber number as a function of Re_f .
- Figure 11. Dimensionless Force Ratio as a function of Re_f .
- Figure 12. Experimentally measured film separation by mass correlated to the calculated Force Ratio for various gas phase and liquid phase flow conditions. Surface tension is shown in parenthesis.
- Figure 13. Predicted effects of wall angle of the onset of film separation for various gas phase and liquid phase flow conditions.

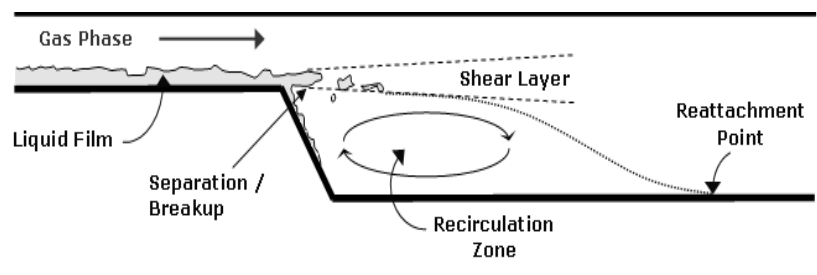


Figure 1. Schematic of shear driven film interaction with separated gas phase flow resulting in partial film separation from the substrate at the corner.

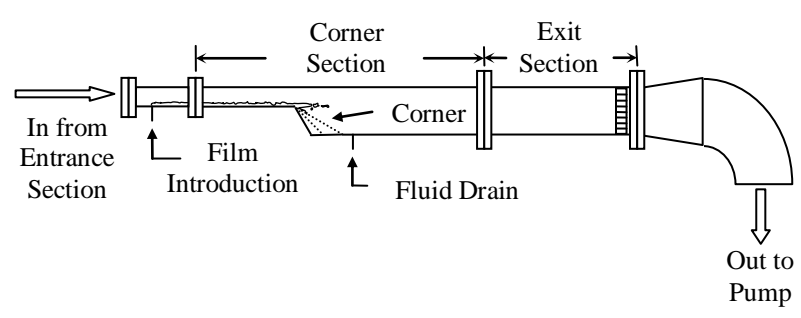


Figure 2. Schematic of test section.

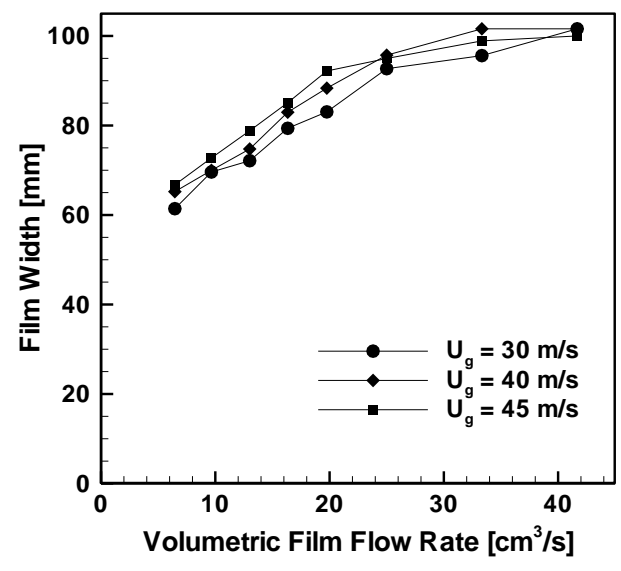


Figure 3. Film width near the test section corner as a function of film flow rate and gas phase velocity.

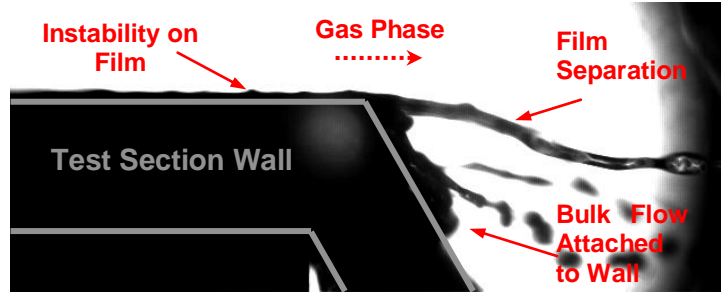


Figure 4. High speed imaging (2000 frames per second) of the film interaction with the separated gas flow at the test section corner.

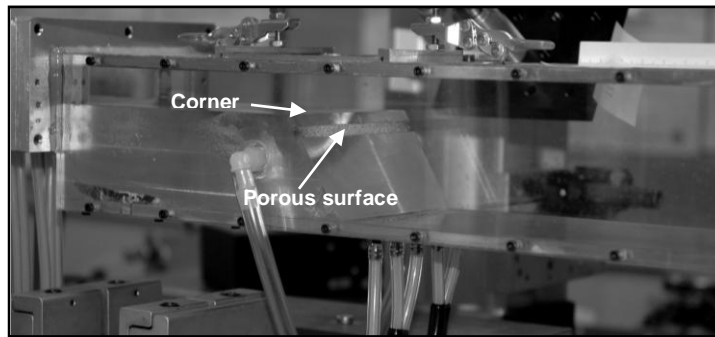


Figure 5. Picture of test section showing porous surface where film which remains attached after the corner is removed.

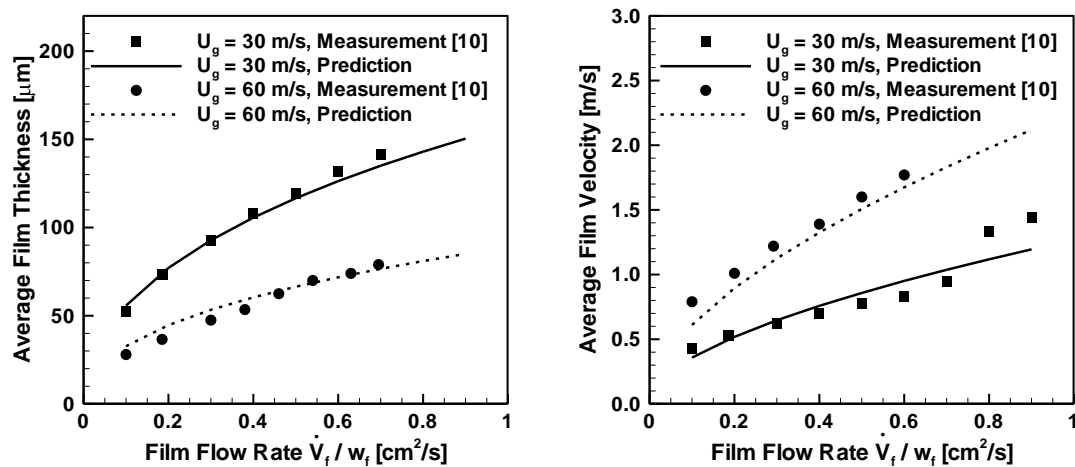


Figure 6. Comparison of the results of the rough wall model used in this work and the experimental results reported in Wittig et al. [10].

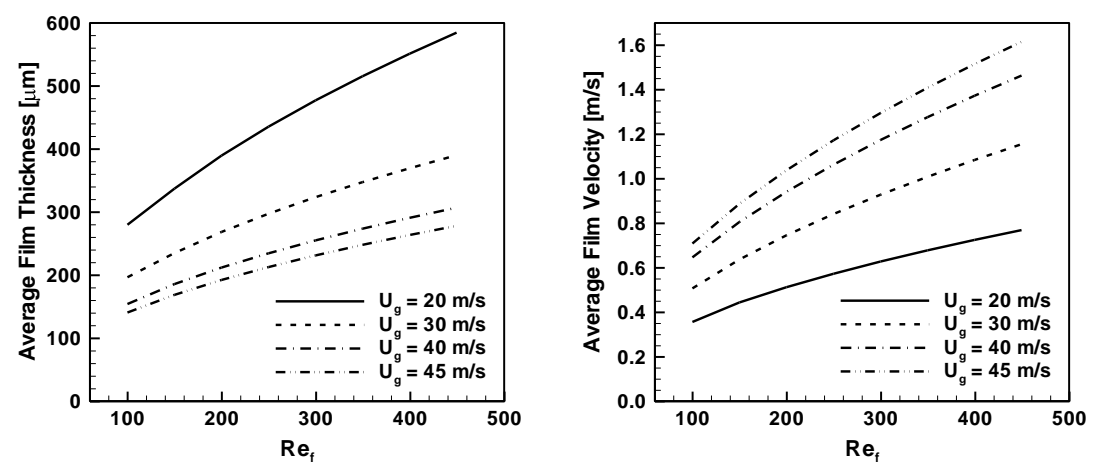


Figure 7. Typical results from the rough wall model used to predict film characteristics before the corner in the test section.

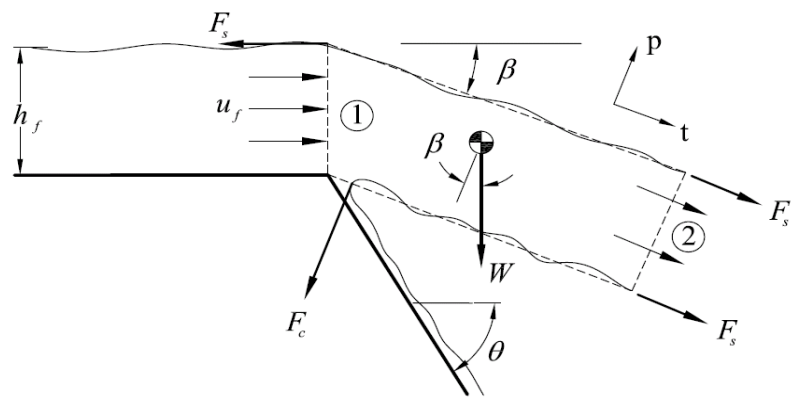


Figure 8. Momentum analysis for a control volume.

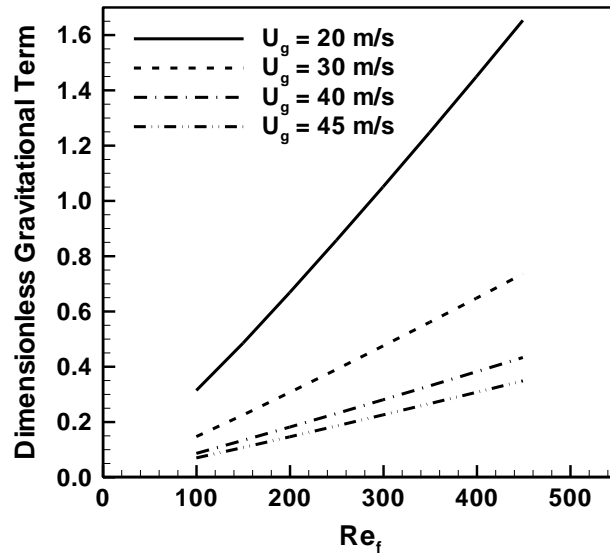


Figure 9. Dimensionless gravitational term from Equation 21 as a function of Re_f .

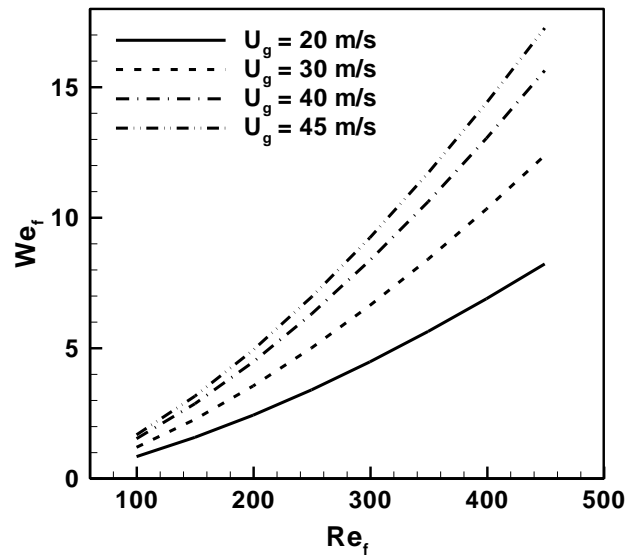


Figure 10. Film Weber number as a function of Re_f .

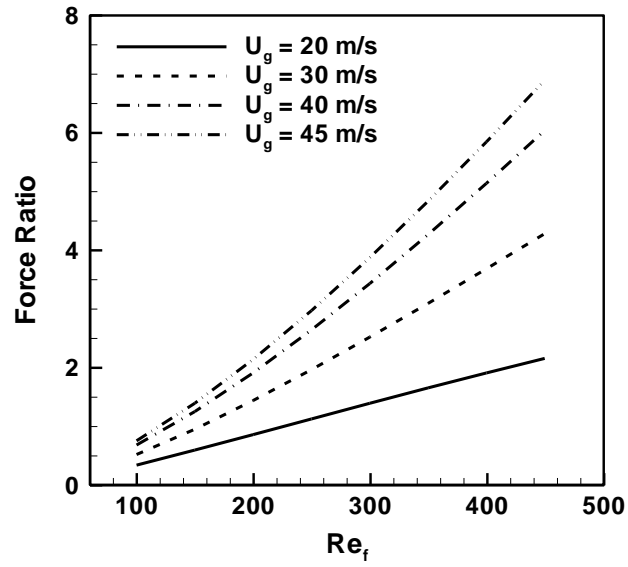


Figure 11. Dimensionless Force Ratio as a function of Re_f .

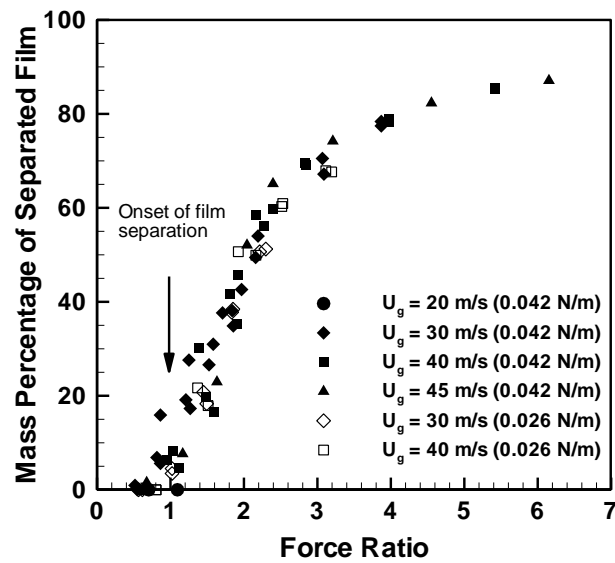


Figure 12. Experimentally measured film separation by mass correlated to the calculated Force Ratio for various gas phase and liquid phase flow conditions. Surface tension is shown in parenthesis.

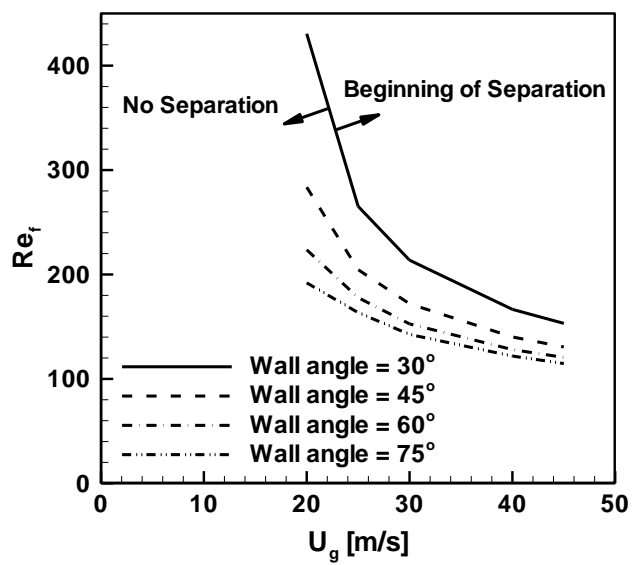


Figure 13. Predicted effects of wall angle of the onset of film separation for various gas phase and liquid phase flow conditions.

Nomenclature

A	=	area
CS	=	control surface
F_c	=	surface tension force at bottom of film
F_{ex}	=	external force
Fr_{hf}	=	film Froude number
F_s	=	surface tension force at top of film
g	=	gravitational constant
h_f	=	film thickness
k	=	turbulent kinetic energy
k_s	=	wall roughness
L_b	=	characteristic length of the film after the corner
\bar{n}	=	normal vector
Re_f	=	film Reynolds number
Re_{ks}	=	roughness Reynolds number
S_ϕ	=	source term
U_g	=	gas phase velocity
\bar{u}_{in}	=	initial fluid velocity vector
u_f	=	film velocity
u_{fs}	=	film surface velocity
u	=	fluid velocity component
v	=	fluid velocity component
\bar{v}	=	velocity vector

\dot{V}_f	=	film volumetric flow rate
W	=	gravitational force
We_f	=	film Weber number
We_{rel}	=	relative Weber number
w_f	=	film width
β	=	separated film angle from the horizontal
Γ_ϕ	=	effective diffusion coefficient
ε	=	dissipation
θ	=	surface corner angle from the horizontal
κ'	=	von Karman constant
μ_f	=	film viscosity
ρ_f	=	film density
σ	=	surface tension
τ	=	shear stress
ϕ	=	corresponding variable
ψ_τ	=	efficiency factor of film roughness
∇	=	gradient
\forall	=	volume

Subscripts

p	=	first grid point
w	=	wall

References

- [1] Felton, P.G, Kyritsis, D.C., and Fulcher, S.K., “Visualization of Liquid Fuel in the Intake Manifold During Cold Start,” Society of Automotive Engineering Technical Paper (952464), 1995.
- [2] Dawson, M., and Hochgreb, S., “Liquid Fuel Visualization Using Laser-Induced Fluorescence During Cold Start,” Society of Automotive Engineering Technical Paper (982466), 1998.
- [3] Landsberg, G., Heywood, J., and Cheng, W., “Contribution of Liquid Fuel to Hydrocarbon Emissions in Spark Ignition Engines,” Society of Automotive Engineering Technical Paper (2001-01-3587), 2001.
- [4] Stanglmaier, R., Li, J., Matthews, R., “The Effects of In-Cylinder Wall Wetting Location on the HC Emissions from SI Engines,” Society of Automotive Engineering Technical Paper (1999-01-0502), 1999.
- [5] Hanratty, T.J., and Theofanous, T. (editors), “Multiphase Flows: An Assessment with a View to the Future,” Colloquium, University of Illinois at Urbana-Champaign, November 5-6, 1994.
- [6] Chang, H.-C., “Wave Evolution on a Falling Film,” Annual Review of Fluid Mechanics, **26**, pp. 103-136, 1994.
- [7] Kriegsmann, J.J., Miksis, M.J., and Vanden-Broeck, J.M., “Pressure Driven Disturbances on a Thin Viscous Film,” Physics of Fluids, **10**(6), pp.1249-1255, 1998.
- [8] Lightfoot, M.D.A., “Atomization of Wall-Bounded Two-Phase Flows,” *ILASS Americas, Proceedings of the 19th Annual Conference on Liquid Atomization and Spray Systems*, Toronto, Canada, May 2006.
- [9] Sattelmayer, T., and Wittig, S., “Internal Flow Effects in Prefilming Airblast Atomizers: Mechanisms of Atomization and Droplet Spectra,” Journal of Engineering for Gas Turbines and Power, **108**, pp.465-472, 1986.
- [10] Wittig, S., Himmelsbach, J., Noll, B., Feld, H.J., and Samenfink, W., “Motion and Evaporation of Shear-Driven liquid Films in Turbulent Gases,” Journal of Engineering for Gas Turbines and Power, **114**, pp.395-400, 1992.
- [11] Himmelsbach, J., Noll, B., and Wittig, S., “Experimental and Numerical Studies of Evaporating wavy Fuel Films in Turbulent Air Flow,” International Journal of Heat and Mass Transfer, **37**, pp. 1217-1226, 1994.
- [12] O’Rourke, P.J., and Amsden, A.A., “A Particle Numerical Model for Wall Film Dynamics in Port-Injected Engines,” Society of Automotive Engineering Technical Paper (961961), 1996.
- [13] Maroteaux, F., Llory, D., Le Coz, J-F., and Habchi, C., “Liquid Film Atomization on Wall Edges – Separation Criterion and Droplets Formation Model,” Journal of Fluids Engineering, **124**, pp. 565-575, 2002.

- [14] Maroteaux, F., Llory, D., Le Coz, J-F., and Habchi, C., “Potential of Inertial Instabilities for Fuel Film Separation in Port Fuel Injection Engine Conditions,” *International Journal of Engine Research*, **4**(1), pp. 11-26, 2003.
- [15] Gubaidullin, A, “Comments on “Liquid Film Atomization on Wall Edges – Separation Criterion and Droplets Formation Model”,” *Journal of Fluids Engineering*, **129**, pp. 665-666, 2007.
- [16] Steinhaus, B.C., Ghandhi, J.B., and Shedd, T.A., “Experimental Investigation of Liquid Film Stripping at a Sharp Corner,” *ILASS Americas, Proceedings of the 20th Annual Conference on Liquid Atomization and Spray Systems*, Chicago, IL., May 2007.
- [17] Thiruvengadam, M., Armaly, B.F., and Drallmeier, J.A., “Shear Driven Liquid Film in a Duct,” Accepted for publication, *Journal of Fluids Engineering*, 2008.
- [18] Gerendas, M., and Wittig, S., “Experimental and Numerical Investigation on the Evaporation of Shear-Driven Multi-Component Liquid Wall Films,” *Journal of Engineering for Gas Turbines and Power*, **123**, pp. 580-588, 2001.
- [19] Tao, W.Q. *Numerical Heat Transfer (2nd edition)*, Xi’an Jiaotong Univ. Press, Xi’an, China, May, 2001.
- [20] Hartley, D.E. and Murgatroyd, W., “Criteria for the Break-up of Thin Liquid Layers Flowing Isothermally over Solid Surfaces,” *International Journal of Heat and Mass Transfer*, **7**, pp. 1003-1015, 1964.
- [21] Murgatroyd, W., “The Role of Shear and Form Forces in the Stability of a Dry Patch in Two-phase Film Flow,” *International Journal of Heat and Mass Transfer*, **8**, pp. 297-301, 1965.
- [22] Penn, D.G., Lopez de Bertodano, M., Lykoudis, P.S., and Beus, S.G., “Dry Patch Stability of Shear Driven Liquid Films,” *Journal of Fluids Engineering*, **123**, pp. 857-862, 2001.
- [23] Arai, T. and Hashimoto, H., “Disintegration of a Thin Liquid Sheet in a Concurrent Gas Stream,” *Proceedings of the Third International Conference on Liquid atomization and Spray Systems*, London, 1985.
- [24] Wang, Y-P., Thiruvengadam, M., Drallmeier, J.A., and Armaly, B.F., “A Comparison of Models for Shear-driven Liquid Film Separation Around a Corner,” *ILASS Americas, Proceedings of the 18th Annual Conference on Liquid Atomization and Spray Systems*, Irvine, Ca., May 2005.
- [25] Owen, I. and Ryley, D.J., “The Flow of Thin Liquid Films Around Corners,” *International Journal of Multiphase Flow*, **11**(1), pp. 51-62, 1985.

PAPER 2**Measurement of the Mean Film Thickness of Dynamic Shear-driven Thin Liquid Films Using Optical Interferometry****M.A. Friedrich, H Lan, N.E. Wilke, J.A. Drallmeier, and B.F. Armaly****Department of Mechanical and Aerospace Engineering****Missouri University of Science and Technology****1870 Miner Circle****Rolla, MO 65409-0050 USA****Abstract**

The dynamics of thin liquid films that develop on a solid surface and are driven by an adjacent gas flow have many engineering applications including fuel systems in internal combustion engines, liquid atomizer systems, refrigerant flows in evaporators, and film drag over wetted surfaces. However, the lack of a reliable, non-intrusive technique to capture and analyze the characteristics of the film limits current efforts to achieve an accurate model of the film flow. An experimental facility has been constructed, which enables a controlled development of a thin shear-driven film and subsequent analysis of the film characteristics. A primary parameter for understanding and predicting the film behavior is the determination of the average film thickness. An interferometric film thickness measurement technique, along with a Fast Fourier Transform based post-processing method, are presented for use as a diagnostic tool to obtain the average film thickness of these dynamic films with surface instabilities. The approach centers on the concept that one single, unique interferometric fringe spacing will exist over an image with a valid film thickness measurement. Important considerations for accurate measurement of the film thickness are discussed along with experimental results showing the capability of the technique to capture the average thickness of the shear-driven film. Control variables include gas and film velocities, film flow rate, and film surface tension.

1. Introduction

The dynamics of thin liquid films that develop on a solid surface and are driven by an adjacent gas flow have many engineering applications including fuel systems in internal combustion engines, liquid atomizer systems, refrigerant flows in evaporators, and film drag over wetted surfaces. Key to the development and validation of useful engineering models to simulate these flows is the measurement of the average film thickness on surfaces similar to those in each application. However, the characteristics of the solid substrate surface as well as the instabilities on the surface of the shear-driven film present significant challenges to techniques used to measure the film thickness. The nature of the shear-driven flow causes Kelvin-Helmholtz instabilities to exist on the top surface of the film. These instabilities cause the film thickness as well as the angle of the film surface to be constantly changing, making it very difficult to obtain a film thickness measurement. Also, measuring the film thickness on a variety of substrate surfaces limits the number of techniques available because access to the film is limited. Therefore, the lack of a reliable, inexpensive, non-intrusive technique to capture the mean film thickness on a variety of substrate surfaces motivates the current work.

2. Background

Thin film thickness measurements have been made using a wide variety of techniques. Many of the techniques have been developed for use with water because of its conductivity. Capacitance sensors used by Klausner et al. [1] measure the capacitance across the film to determine the film thickness and require an access point both above and below the film. Conduction probes used by Suyari and Lefebvre [2] are configured in a similar fashion, but instead use the conductance across the fluid to determine the film

thickness. These methods are intrusive and require accurate, high-resolution equipment to obtain a reliable result, making them not well-suited for flows with surface instabilities.

Another class of non-intrusive techniques includes those that incorporate a laser light source. Laser-induced fluorescence (Schagen and Modigell [3], Maroteaux et al. [4], Yang and Melton [5], Driscoll et al. [6], Shaw II et al. [7], Ting [8]) requires one access point and uses either the fluorescent components in the liquid or an added dopant as the source of fluorescence. Images are captured using a CCD camera and analyzed to determine the film thickness. Laser light absorption uses a similar approach, but uses light absorption instead of fluorescence and requires two optical access points, usually above and below the film. (Mouza et al. [9], Barter et al. [10,11], Wittig et al. [12]). Another technique makes use of the total internal light reflection which occurs at a liquid-vapor interface because of the refractive index difference between the liquid and vapor (Hurlburt and Newell [13], Shedd and Newell [14]). The distance between the light source, which is perpendicular to the film, and the reflected light rays is proportional to the film thickness. Therefore, high-speed images are also captured for this technique and analyzed to determine the film thickness. This technique requires only one access point, but it must be below the film. Having an access point below the film greatly restricts the surface materials that can be used to support the film and hinders the use of these laser based techniques for many engineering applications.

Other methods used to determine film thickness include microwave absorption used by Roy et al. [15], and laser focus displacement used by Takamasa and Hazuku [16].

All of these methods differ in ease of use, calibration, accuracy, cost and intrusiveness, and as such have advantages and disadvantages depending upon the application.

For the current application to shear-driven films with surface instabilities, the system must be able to obtain an accurate mean film thickness for a variety of substrate surfaces despite the film surface instabilities. The interferometric approach is well suited for this type of measurement because it is a non-intrusive point measurement, needs only one access point, requires minimal calibration, and is relatively inexpensive. The interferometer approach was initially developed by Ohyama et al. [17], with improvements having been made with the technique by Nosoko et al. [18] and most recently by Kelly-Zion et al. [19] who measured the transient thickness of an evaporating film. As the published literature does not indicate any temporally and spatially resolved thickness measurements of shear-driven films with surface instabilities made using this method, this paper focuses on an enhancement of the technique reported by Kelly-Zion et al. [19] by application of this technique to the measurement of the average thickness of dynamic shear-driven films.

3. Theory of Technique

The interferometric technique makes use of the phase shift between the reflection of incident light from the top and bottom surfaces of the film. As shown in Figure 1, when the light approaches the film over a small range of incident angles, a portion of the incident light reflects at the top surface of the liquid film and a portion transmits through the film and reflects at the bottom surface. The refraction of light in the film causes the light leaving the film to interfere either constructively or destructively, depending on

whether the change causes the light waves to be in phase or out of phase. For one light ray incident on the film at an angle θ_i , the phase difference, δ , is calculated to be

$$\delta = \frac{4\pi t}{\lambda_0} (n_l^2 - n_g^2 \sin^2 \theta_i)^{1/2} \pm \pi \quad (1)$$

where t is the film thickness, λ_0 , is the wavelength of light, and n_l and n_g are the indices of refraction of the liquid film and gas respectively. [19]

For light that is incident over a range of angles, a series of light and dark fringes appear in the reflected light because of the interference. Nosoko et al. [18] developed the following to compute the film thickness from the number of fringes, F , which appear in a specified field of view on the reflected light side:

$$t = \frac{\lambda_0 F}{2n_l (\cos \beta_1 - \cos \beta_2)} \quad (2)$$

where β , the angle of refraction, is defined by Snell's law as

$$\sin \beta = \frac{\sin \theta_i}{n_l} \quad (3)$$

The distance from the film to the field of view is critical in this measurement and is included in the $(\cos \beta_1 - \cos \beta_2)$ term of Equation (2).

4. Experimental Facility

4.1 Shear-driven Film Test Section

The flow facility used in this experiment was developed in order to study shear-driven liquid film propagation and the ensuing separation and break-up at a sharp expanding corner (Friedrich et al. [20], Lan et al. [21]). The flow system consists of a four part test section mounted to an optics table platform. Flow is pulled through the test section using a large liquid ring vacuum pump and flow rates through the test section are

determined using a laminar flow element. Corrections are made for local temperatures and pressures resulting in uncertainties of less than 3% in the measured gas flow rate.

There are four parts to the rectangular test section; three of those parts are shown in Figure 2. A 1.43 m long entrance region (not shown) provides for two-dimensional flow span-wise across the test section at the point of film introduction. The dimensions of the test section at the point of film introduction and up to the corner are 2 cm tall by 10 cm wide giving an aspect ratio of 5. The liquid is introduced through a porous medium on the bottom wall in the film introduction section. Simulations indicate that, with the entrance region, flow should be 2-dimensional with this aspect ratio (i.e. limited wall effects) for the center 7.5 cm of the test section. It is over this center 7.5 cm width that the film is introduced. The flow of liquid into the test section is quantified on a volumetric flow basis and measured using a rotometer with an uncertainty of 2.5%. Unless shown otherwise, for the results presented, the liquid was water with the addition of a surfactant (Surfynol 465) at 0.1% by mass which results in a surface tension of 0.042 N/m.

Optical access is provided from the top, 40mm upstream and 40mm downstream of the corner, to enable measurement of an average film thickness before the corner. The film thickness measurement is made 5 mm upstream of the corner so that the corner has negligible effect on the liquid film flow. The length of the duct from the point of film introduction to the corner is 23 cm. After the corner, the duct has an aspect ratio of 1.429 wherein an exit section provides for a transition from the test section to the 10.2 cm diameter piping which runs to the liquid ring pump. Great care is taken to ensure the test section is horizontal to prevent biasing of the film flow.

4.2 Optical Hardware Configuration

4.2.1 *Transmitting Optics*

The optical configuration of the film thickness measurement system is shown in Figure 3. A 10 mW HeNe laser is collimated to approximately a 20 mm diameter. A 100 mm focal length lens is currently used to develop a spot size of less than 0.01 mm diameter on the film. This spot size determines the spatial resolution of the system and also has an effect on the background noise prevalent in the images, therefore, minimizing the spot size when configuring the system is essential to achieve good quality images. The distance from the focusing lens to the test section bottom wall was set initially by measurement with a digital caliper, and then the transmitting optics were fine tuned to achieve the minimum spot size by viewing images captured with no film on the solid substrate and adjusting the distance with a micrometer adjustment to minimize the background noise.

As shown in Figure 4, the nature of the shear-driven flow causes Kelvin-Helmholtz instabilities to exist on the top surface of the film. These instabilities cause the film thickness as well as the angle of the film surface to be constantly changing relative to the solid substrate wall. The application of the interferometric technique to this dynamic film case is much different than a static film; therefore, both the optical configuration and the image acquisition system must be optimized for use with these dynamic films.

The angle of incidence affects the amount of light reflecting off of the top and bottom surfaces of the film (i.e. the Fresnel relations). If more light is reflected off of one surface than the other, then the interference pattern will be dominated by the light with

the greater reflection. Therefore, an equal amount of light reflected from each surface would give the highest visibility to the interference pattern. In the study by Nosoko et al. [18], it was shown that the fringe density in the image was also affected by the incidence angle. In that study the incidence angle was chosen to achieve the appropriate fringe density for a given film thickness to ensure roughly 10-50 fringes on the image target. To adjust fringe density in this study, however, the receiving optics, not the angle of incidence, were manipulated. For the dynamic case there are instabilities present on the surface of the dynamic film that also affect the reflection of the light in and out of the film. As shown in Figure 5, using a smaller angle of incidence with respect to the vertical axis minimizes the effect of these instabilities by decreasing the distance between where the light enters and exits the film, thus increasing the probability that the surface will be at the same angle for both points. A smaller angle of incidence also reduces the size of the entrance point needed to get the laser light in and out of the test section.

A test matrix was composed such that the parameters for image quality and angle of incidence could be analyzed simultaneously. A sample of 250 images was taken from each test case and analyzed to determine the number of images with discernable fringe patterns. With all other parameters being equal, the cases with incidence angles of 30° had significantly more images with a discernable fringe pattern than all other incidence angles tested and these cases also had the best visual image quality. Considering the effects described above, the shallow 30° incidence angle gives a relatively short distance between the entrance and exit points of the light without sacrificing the contrast between the light and dark fringes in the interference pattern. Therefore, this angle was chosen as the optimum incidence angle for all test cases reported in this study.

4.2.2 *Receiving Optics*

The light reflected from the film, which forms the interference pattern, is imaged on an image target and captured using high speed imaging (see Figure 3). Temporal resolution is determined by the rate at which the fringe imaging takes place. For the results shown here, a high frame-rate camera, a Photron 1280 PCI, was used operating at 4000 frames per second.

In the study by Kelly-Zion et al. [19] frosted glass was used as the image target, however, due to the finish on the frosted glass, the resolution of the fringe pattern captured with the high-speed camera was less than ideal for image post-processing because of the presence of random bright pixels within the image. Therefore, in order to improve the image quality for post-processing a neutral density filter was used in this study as the image target. A comparison of the two image targets using a sapphire disk as a representative film is shown in Figure 6. Using the neutral density filter as the image target increased the visibility of the Airy rings (caused by dust or imperfections on the camera lenses), but reduced the noise which can be seen in the frosted glass image. The post-processing algorithm could more accurately determine the film thickness despite the Airy rings than it could with the background noise.

The field of view used to determine the number of fringes in the interference pattern can be defined by the focusing lens on the transmitting optics side and/or any aperture used in the receiving optics. When using the focusing lens, the field of view is defined by the edge of the interference pattern which corresponds to the extreme angles of the reflected light. When using an aperture in the receiving optics, however, the field of view is defined by the edge of the aperture. In this study an aperture was used in the

receiving optics because the edge was more clearly defined and invalid patterns, caused by a surface angle on the film greater than two degrees from horizontal, were blocked by the aperture.

It is important to note that the interferometric technique, as configured here, will only display fringes on the image target for film surfaces nearly parallel with the bottom surface of the test section. For example, measurements of a stationary drop placed on the test section bottom wall (Figures 7 & 8), indicated that the fringe pattern was only observable for film surfaces less than two degrees out of parallel with the bottom wall. If the surface is outside of two degrees from parallel the interference pattern is reflected outside of the viewing area set by the aperture on the image target. This characteristic of the optical setup helps to filter out images that would not give an accurate film thickness measurement anyway because the interferometric technique requires a nearly parallel surface for accurate thickness measurements. Hence, for a film with traveling waves, this implies that the film thickness will only be recorded for wave peaks and troughs and not the continuous film profile. However, a time series of film peak and trough thickness information can then be used to obtain an average film thickness.

The same test matrix used to analyze the angle of incidence was also used to analyze the fringe pattern image quality. The parameters affecting image quality include the camera aperture setting, camera shutter speed, and sensitivity. The camera aperture setting and shutter speed are intimately related as observed during the testing. Therefore, changing one required changing the other in order to obtain a good quality image. The image quality was determined by a visual inspection of the fringe patterns, looking for

fringe clarity, contrast, and intensity. The optimal settings were chosen to maximize contrast with a shutter speed of 1/4000 second.

5. Image Analysis and Frequency Determination

5.1 Objectives and Key Ideas

The objective of the interferometric film thickness measurement system is to determine the average film thickness for a given set of flow conditions. However, the identification of images which contain valid interference patterns, and the subsequent analysis of those images to determine the film thickness, is much different in this application to dynamic films than most previous applications of this technique. A comparison of typical fringe patterns is shown in Figure 9. When using this technique to determine the instantaneous film thickness of a dynamic film, the fringe patterns that are captured do not typically look like the images captured for a static film. The fringe pattern for a static film exists in the entire image, whereas for a dynamic film the fringe pattern usually exists only in a section of the image. In the static film the top surface is smooth, parallel with the bottom wall, and unchanging; therefore, the optical system can be adjusted to capture the fringe pattern in the entire image, as shown in Figure 9c. When measuring a dynamic film, however, the top surface of the film has many time varying instabilities. The change in angle between the incident light and the top surface of the film with the arrival of an instability causes the fringe pattern to be shifted on the image screen resulting in a “partial” image, similar to the one shown in Figure 9d. The bottom surface of the film also has an effect on the image in the form of background noise as can be seen in Figure 9b. This background noise is prevalent in the measurement of both the static and dynamic films due to surface roughness of the solid

wall substrate. A comparison of these image characteristics along with an image captured using a sapphire disk as a representative film is shown in Figure 9. Also, as previously discussed, a fringe pattern does not exist in every frame like the static case because of the instabilities present on the surface of the film. Therefore, automatic detection of frames with a discernable fringe pattern and the subsequent determination of fringe spacing for the valid frames present a unique challenge.

Since the interferometric technique has the ability to capture only the peaks and troughs of the film, an appropriate frame rate must be used with the aim of capturing as many peaks and troughs as possible. As mentioned previously, the required frame rate was chosen by determining the frequency of the surface instabilities for this flow from high speed imaging similar to Figure 4. The required imaging rate was calculated to be 4000 frames per second for the dynamic film being considered. To capture a significant data sample at this high frame rate leads to very large files, which must be stored for post-processing. For example, using a frame rate of 4000 frames per second, a two second sample would contain 8000 images with a 128X640 image resolution, and would require approximately 640 megabytes of storage space.

With this time series of images, the post processing protocol must be able to discern images with and without fringes. Because of the background noise in the captured images and instabilities on the surface automatic fringe pattern detection is a challenge. The level of background noise can be somewhat controlled by the camera and image software settings (shutter speed, sensitivity, gamma, etc.), but it cannot be eliminated. Therefore, the automated image analysis approach must be able to ignore this background noise, identify images with a fringe pattern (which may only exist over a

portion of the image due to instabilities), and then determine the film thickness from the fringe spacing.

5.2 Image Identification and Analysis Protocol

The initial approach to identify images with fringes and subsequently determine the number of fringes in an image was to view each image in sequence and then count fringes by hand. It took approximately 1 hour per 1000 images to analyze the data using this approach, so an automatic detection and counting process was required to make this technique more efficient and less user-dependent. Therefore, an algorithm written in MATLAB[®] has been developed to accomplish these tasks. Each frame is recorded by the camera as a bit-map file and stored in sequence by the camera software. The algorithm then examines each image to determine if a fringe pattern exists, and if it does, it determines the fringe spacing in order to calculate the corresponding film thickness.

The *key* to this technique is the fact that each frame with a discernable fringe pattern will have one unique characteristic fringe spacing (frequency) corresponding to the thickness of the film at that instant. Images with no fringe pattern should have no dominant frequency. It was decided that the best method for both detecting and counting these fringes would be to employ a Fast Fourier Transform (FFT) approach to take advantage of the dominant frequency. A block diagram of the algorithm protocol is shown in Figure 10.

5.3 Image Processing Algorithm

5.3.1 *Identification of Images with Fringes*

The initial approach performed an FFT on every column of pixels in the image in order to determine the dominant frequency across the image. However, results were poor using this method because of the intensity variation from pixel to pixel in the one column caused by the background noise as well as the Airy rings. Subsequent approaches have employed pixel averaging methods. The human eye is incapable of detecting the intensity of every single individual pixel column in the image array but instead blurs over a spatial region. The mathematical averaging of columns is intended to duplicate that effect. In these trials, between three and five pixel wide columns have been combined using the intensity from the raw image, pre-Fourier transform, and then forwarded for further analysis.

An FFT (see Figure 11) is done on each averaged column and a signal-to-noise criterion (approximately 10 to 1) is applied in order to determine if there is a dominant frequency in the averaged column. As can be seen in Figure 11, the number of lines on the FFT plot corresponds to the number of averaged columns. For instance, if there were 125 columns in the raw bitmap image and every five columns were averaged together, there would be 25 averaged columns, so there would be 25 lines on the FFT plot. Every averaged column will not have a dominant frequency because of the noise in the image as discussed previously. Therefore, a tunable parameter has been incorporated to set the number of columns that must meet the signal-to-noise criterion and have a similar dominant frequency in order to be considered a valid fringe pattern and to determine the

dominant frequency of the image. Typical values range from 25 to 30% of total averaged columns. If this parameter is not met, then the image is skipped.

5.3.2 Film Thickness Determination from Fringe Spacing

Using the FFT approach does not give the total number of fringes (i.e. fringe count) in the image like the traditional interferometric application. Instead it gives the *fringe spacing* which can also be used to determine the film thickness given an accurate determination of the image height. Consequently, the next step after identification of images with fringes is the determination of this fringe spacing.

The advantage of using the FFT approach is that the data used to identify the image as being valid is also used to determine the fringe spacing. Once the dominant frequencies are determined for each averaged set of columns, the resulting values are compiled into a histogram, as in Figure 12. As is evident in Figure 12, more than one frequency may exist in the image, but the dominant frequency for the image is calculated by averaging the column frequency values within the largest bin and the two bins on either side of it. From this dominant frequency (fringe spacing), a calculation of the film thickness is made.

Results from this approach have been successful at determining the mean film thickness of a sample set of images with discernable fringes to within 10-15% of measurements done manually (~8000 images captured in a 2 second time series). Figure 13 shows a comparison of the distribution of film thickness used to determine the mean for a set of images using both the FFT and manual processing methods. The distribution of the film thickness using the manual processing method is more dispersed, most likely due to the user including several invalid images that were outside of the dynamic range of

the FFT method. The manual method does have a user imparted bias and is not being considered as a “correct” measurement, but as an alternative approach for image processing. The distribution of the percent error between the manual processing method and the FFT post-processing method showed good agreement between these methods for a single image, with most images having an error of 20% or less. Therefore, using the FFT analysis and discrimination approach greatly increases the ability to analyze results quickly and with less user imparted bias.

5.4 System Dynamic Range

The dynamic range of the measurement system is the range of film thickness values that the system is able to measure with a given configuration. In this study, the dynamic range was determined by both the optical system settings as well as the numerical Fourier transform post-processing analysis method. Changing the receiving optical system will alter the correlation between fringe spacing and film thickness. The distance from the film to the image target is directly proportional to the fringe spacing, as can be seen in Equation (2) $[(\cos\beta_1 - \cos\beta_2)]$ and is *critical* to determining the film thickness. By taking advantage of this relationship, the dynamic range of the system can be altered to match the expected film thickness range and the analysis method.

One limiting factor in the numerical analysis of the fringe spacing is the resolution of the high speed camera. The objective is to have at least five pixels per fringe. Changing the distance between the target and the camera changes the fringe spacing in the image and also the number of pixels per fringe. Therefore, setting this distance to maximize the image size (determined by the external aperture) within the camera window gives the highest resolution or the maximum number of pixels per fringe.

The images captured were all of the same height (640 pixels). The fringe spacing was smaller for thicker fluid films, so fewer pixels would represent each fringe. As previously discussed, each fringe must be represented by multiple pixels. For the current optical settings using water as the fluid, 120 fringes over the entire image height was representative of 1032 μm thickness. This corresponds to around five pixels per fringe over 640 pixel long columns. Therefore to ensure accurate fringe representation without aliasing, 1000 μm was chosen as the dynamic range upper limit in this study.

The minimum of the dynamic range was determined by the low-end noise of the Fourier transform output, as shown in Figure 14, which was caused by the windowing of the image data along with the background noise in the image. The film thickness is determined based on the maximum value in the frequency spectrum; therefore, a cutoff was chosen such that the noise did not cause a false thickness value at very low frequency. Techniques such as offsetting the image pixel values were used to minimize the low frequency noise, but were not successful in eliminating it. Through careful examination of the FFT results for several trial experiments as well as for the sapphire disk used as a representative film, a value of 100 μm was chosen as the dynamic range minimum for this study. Values corresponding to a film thickness lower than this value were not distinguishable from the low range noise in the FFT output. It should be noted that the minimum of 100 μm is not the thinnest film measurable with this technique. By changing the receiving optics, as previously discussed, the dynamic range minimum can be altered to match the desired film thickness range.

6. System Validation

Validation of the film thickness optical system was performed using two methods. First, a sapphire disk of known thickness was measured at a nominal 508 μm which was within the manufacturer's uncertainty (10%). The second validation was done using a film droplet of known volume on the test section surface, as shown in Figure 7. The thickness was measured at several points across the droplet and these values were used to calculate the droplet volume (Figure 8). The measured and calculated volumes had a difference of less than 2%.

7. Experimental Results

Film thickness experiments were conducted for gas phase velocities of 20, 30, and 40 m/s and liquid film flow rates of $\sim 6\text{-}16 \text{ cm}^3/\text{s}$, resulting in Reynolds numbers for the liquid film, Re_f , between 100 and 500, for each gas phase velocity. The film Reynolds number was based on the volumetric flow introduced to develop the film, \dot{V}_f , and the measured film width, w_f , at each flow condition:

$$Re_f = \frac{\dot{V}_f \rho_f}{w_f \mu_f} \quad (4)$$

A time series thickness measurement for a single flow condition (30 m/s gas phase and $13 \text{ cm}^3/\text{s}$ liquid flow rate) is shown in Figure 15. The total number of frames in the data set is 8192 (set by the imaging software), which is slightly over a 2 second sample, imaged at 4000 frames per second. The total number of valid frames, or frames containing a discernable fringe pattern, for this data set was ~ 200 , approximately 2.5% of the total number of images collected for the set.

As previously mentioned, the optical system is able to capture a valid image only when the surface of the film is within two degrees of parallel with the bottom wall. Given the approximate velocity of the instabilities and the time period between the instabilities on the surface of the film, one can calculate the maximum number of valid fringes to expect, assuming a sinusoidal behavior for the surface instabilities. High-speed imaging of the film, as shown in Figure 4, shows an approximate time period of five milliseconds and an approximate velocity of 1 meter per second for the surface instabilities. Given these parameters and the two degree parallelism requirement, the maximum number of valid fringes to expect is ~300 out of 8000 or approximately 5% of the total images captured. Therefore, the number of valid images obtained in the experiments is reasonably close to the maximum number of images one would expect to capture using this technique.

Three film thickness measurement sets were taken for each flow condition in order to determine the repeatability of the measurement system. The results for the 30 m/s - 13 cm³/s flow condition are shown in histogram format in Figure 16. Though the number of valid thickness measurements in each set differs, the average film thickness values for each experiment are within 10%. A representative comparison of the film thickness measurement results for three different flow conditions are also included in Figure 17. Clearly the number of valid thickness measurement points decreases with increasing liquid flow rate (caused by the increased surface instability frequency and velocity as observed with the high-speed imaging), however, the average film thickness does show a slight increase with increasing liquid flow rate as would be expected.

8. Summary and Conclusions

An optical interferometric film thickness measurement system is discussed for use in measuring the mean film thickness of dynamic, shear-driven thin liquid films with surface instabilities. An experimental test facility, designed to study the development of a shear-driven liquid film and its subsequent separation at an expanding corner, was modified to allow access to obtain film thickness measurements using this technique. Validation of the optical system was performed using a droplet of water of known volume, as well as a sapphire disk, obtaining results within the manufacturer's uncertainty of 10%. Optimization of the optical system for use with dynamic films is also discussed.

Automatic identification and subsequent analysis of interference patterns in the captured images is performed using a Fast Fourier Transform approach, which makes use of the concept that one, single unique frequency exists in an image with a discernable fringe pattern, corresponding to the film thickness at that instant. An automated algorithm for identification of images with a pattern has been developed and demonstrated. Important considerations for accurate measurement of the film thickness are discussed along with experimental results showing the capability of the technique to capture the average thickness of the shear-driven film.

Acknowledgements

This work was supported in part by NSF Grant No. CTS-352135.

List of Figure Captions

- Figure 1. Schematic of the reflection of light off of the top and bottom surfaces of a film.
- Figure 2. Schematic of experimental test section.
- Figure 3. Schematic of the optical system for the interferometric film thickness measurement.
- Figure 4. High-speed imaging of film flow showing Kelvin-Helmholtz instabilities on the surface of the film.
- Figure 5. Schematic illustrating how curvature on the film surface affects the light rays exiting the film.
- Figure 6. Comparison of image using frosted glass versus neutral density filter for the image target.
- Figure 7. Image of film droplet used for interferometric film thickness measurement validation.
- Figure 8. Droplet profile measurements used to calculate droplet volume.
- Figure 9. Comparison of images for a) suspended sapphire disk, b) background noise,
- Figure 10. Block diagram of image identification and analysis protocol.
- Figure 11. FFT results from one high-speed image containing a discernable fringe pattern.
- Figure 12. Histogram of dominant frequency/film thickness values for one image.
- Figure 13. Distribution of film thickness values for flow conditions of 20m/s gas phase velocity and 13.01 cm³/s liquid flow rate comparing FFT and manual processing methods.
- Figure 14. Results of FFT showing the low-end noise spike near zero.
- Figure 15. Time series of thickness measurement results for 30 m/s gas phase velocity and 13.01 cm³/s liquid flow rate.
- Figure 16. Distribution of film thickness measurements for three tests at 30 m/s gas velocity and 13.01 cm³/s liquid flow rate.
- Figure 17. Distribution of film thickness measurements for tests at 30 m/s gas velocity and 6.46, 13.01, and 16.34 cm³/s liquid flow rates respectively.

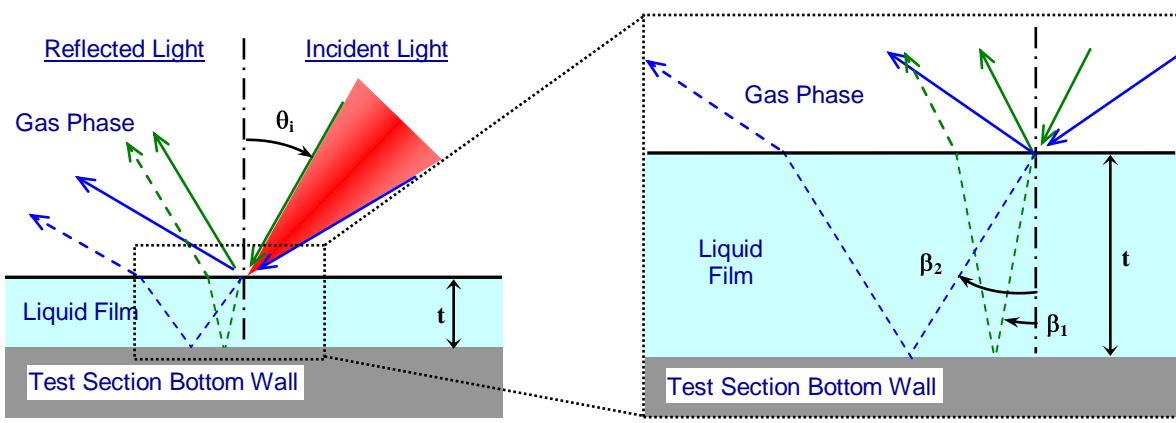


Figure 1. Schematic of the reflection of light off of the top and bottom surfaces of a film.

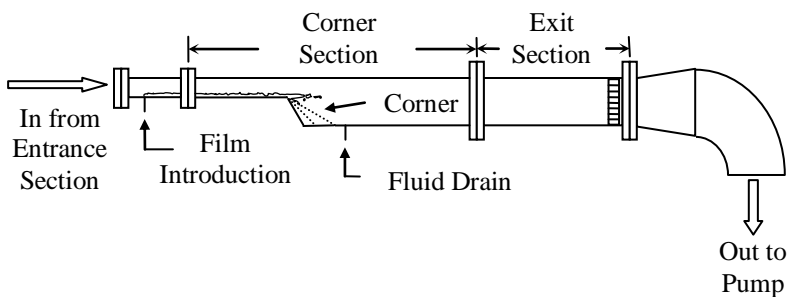


Figure 2. Schematic of experimental test section.

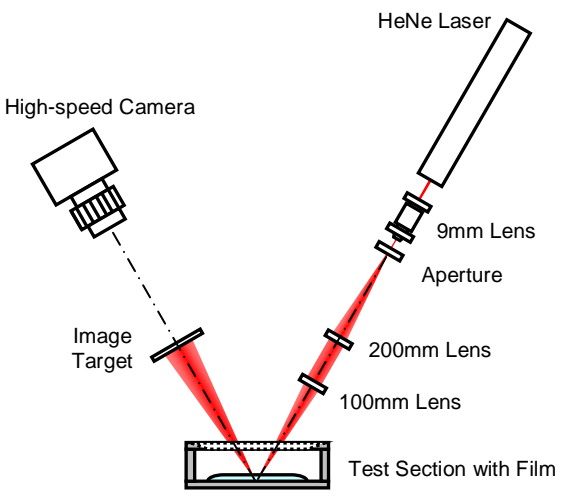


Figure 3. Schematic of the optical system for the interferometric film thickness measurement.

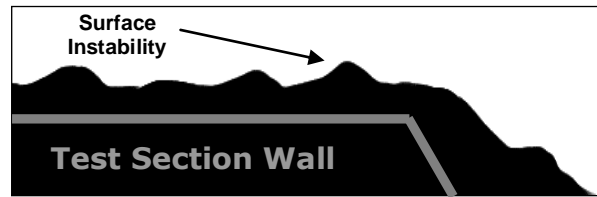


Figure 4. High-speed imaging of film flow showing Kelvin-Helmholtz instabilities on the surface of the film.

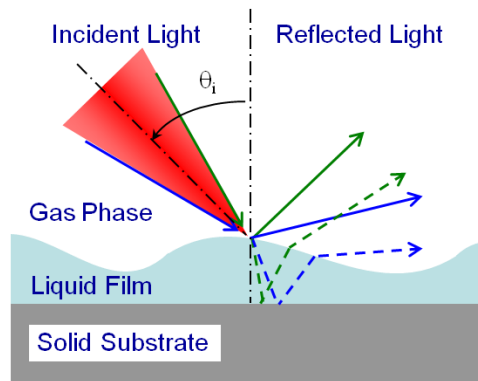


Figure 5. Schematic illustrating how curvature on the film surface affects the light rays exiting the film.

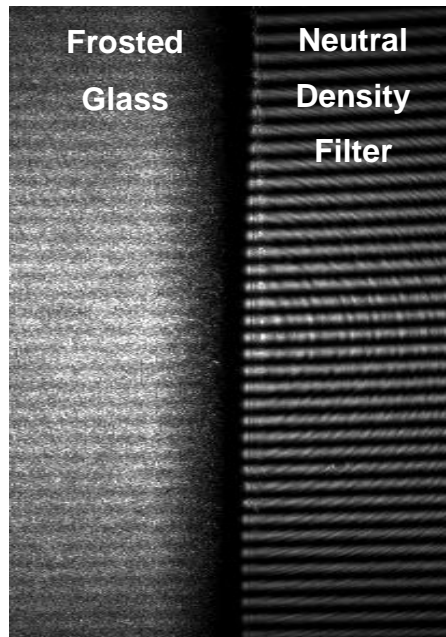


Figure 6. Comparison of image using frosted glass versus neutral density filter for the image target.



Figure 7. Image of film droplet used for interferometric film thickness measurement validation.

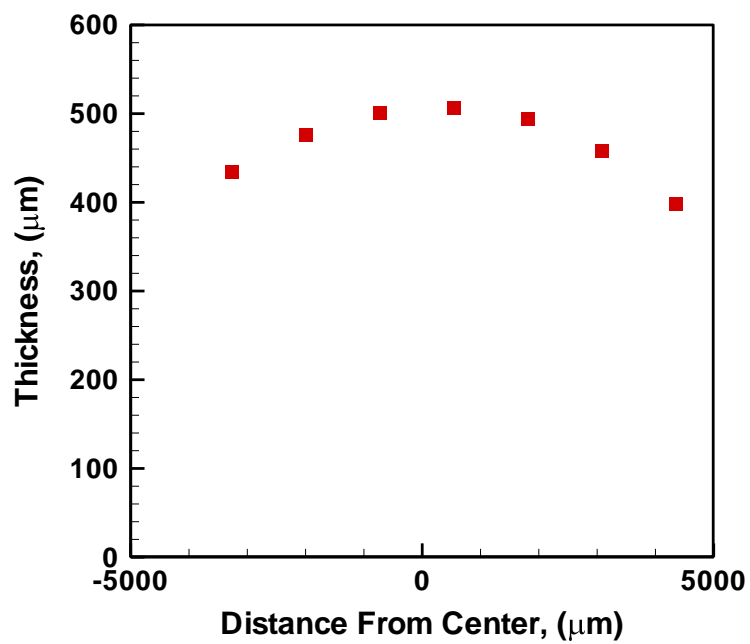


Figure 8. Droplet profile measurements used to calculate droplet volume.

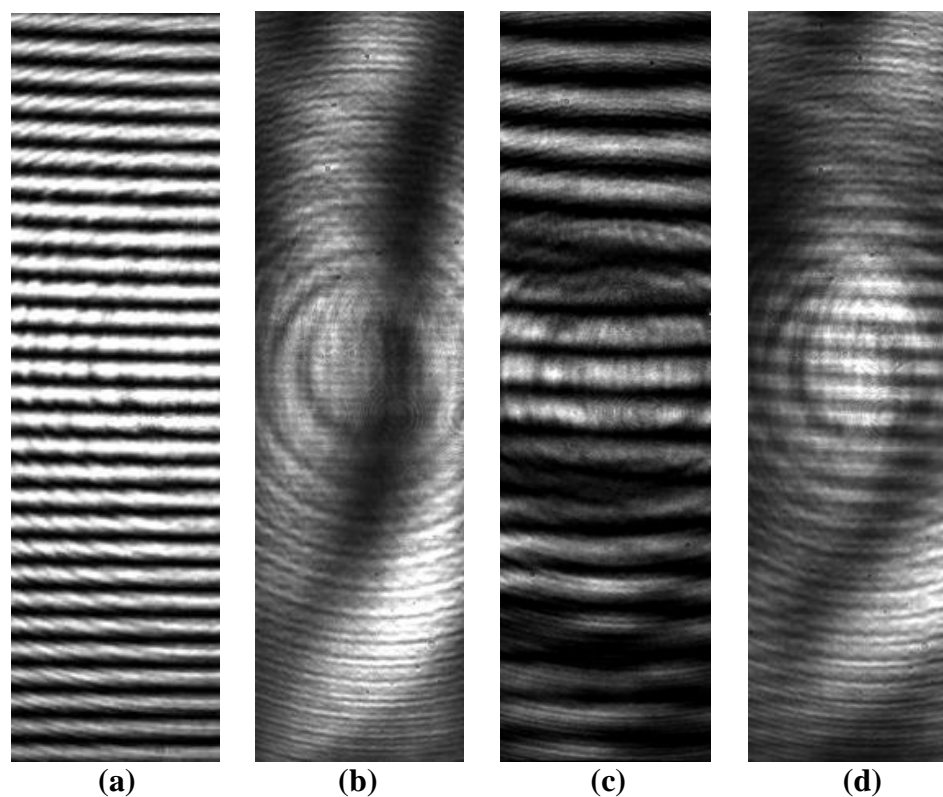


Figure 9. Comparison of images for a) suspended sapphire disk, b) background noise, c) static films, and d) dynamic films.

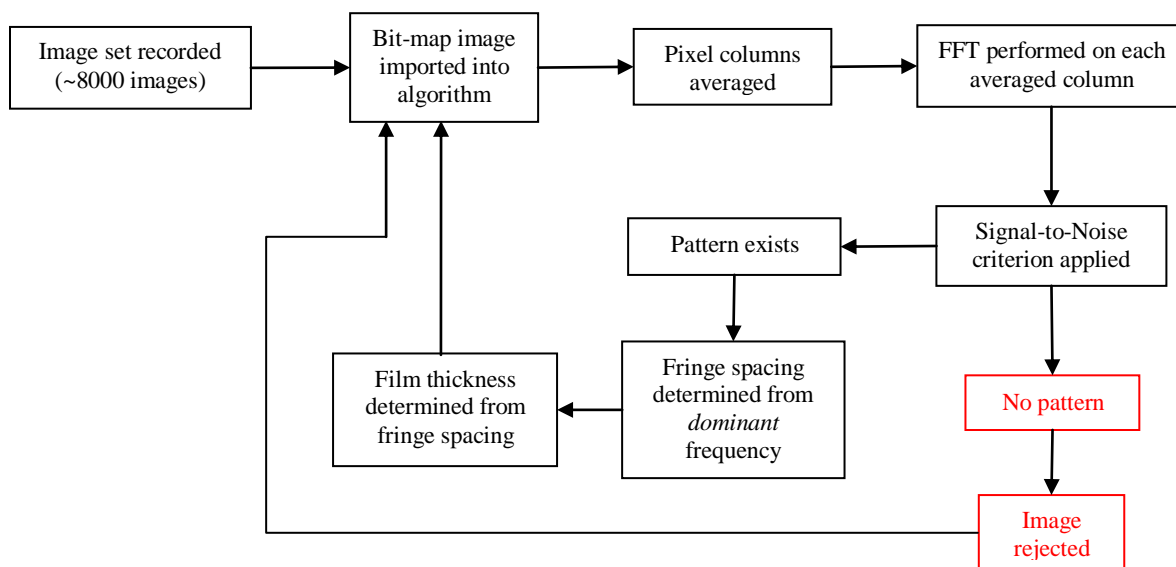


Figure 10. Block diagram of image identification and analysis protocol.

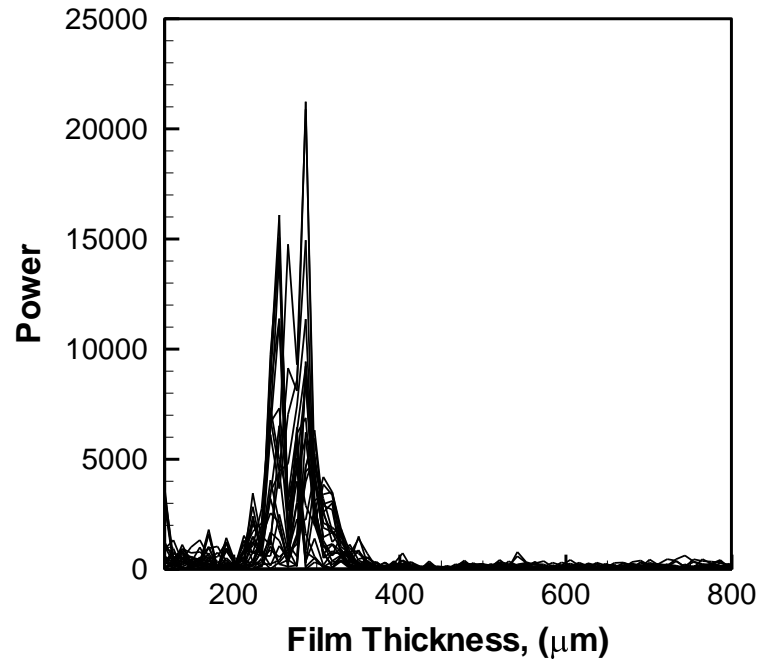


Figure 11. FFT results from one high-speed image containing a discernable fringe pattern.

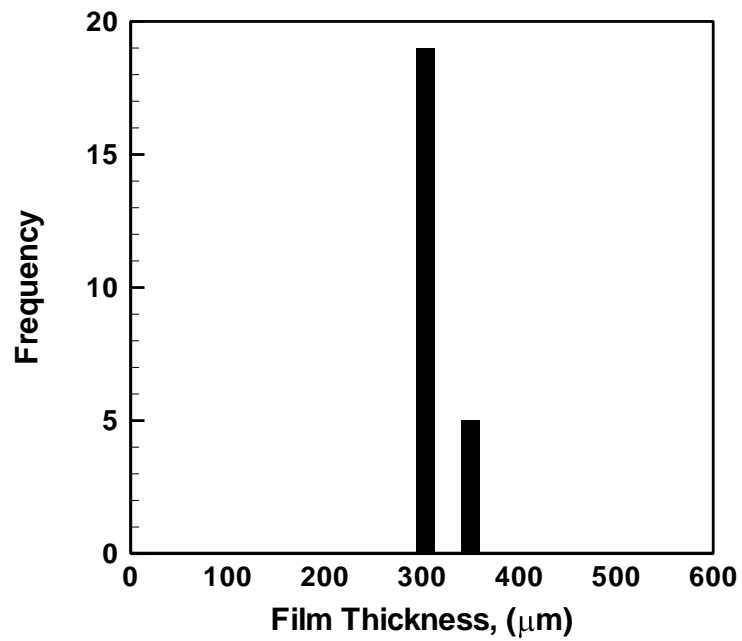


Figure 12. Histogram of dominant frequency/film thickness values for one image.

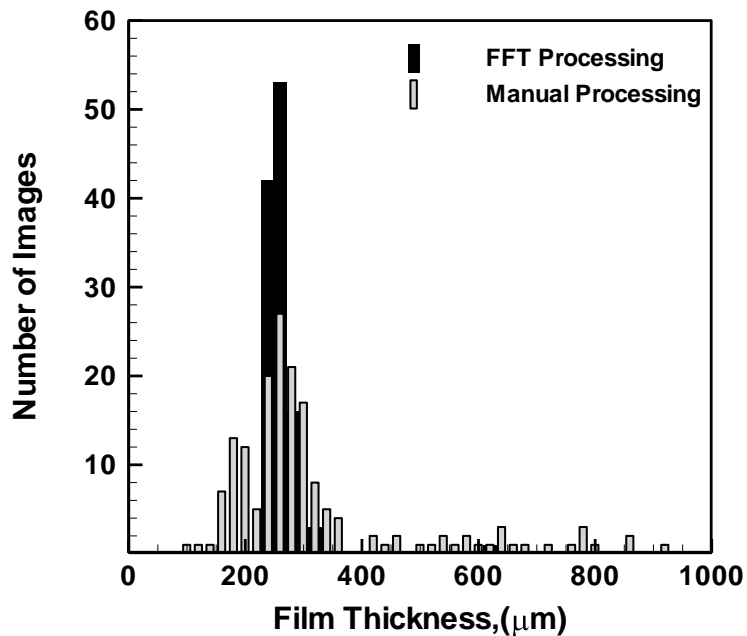


Figure 13. Distribution of film thickness values for flow conditions of 20m/s gas phase velocity and 13.01 cm³/s liquid flow rate comparing FFT and manual processing methods.

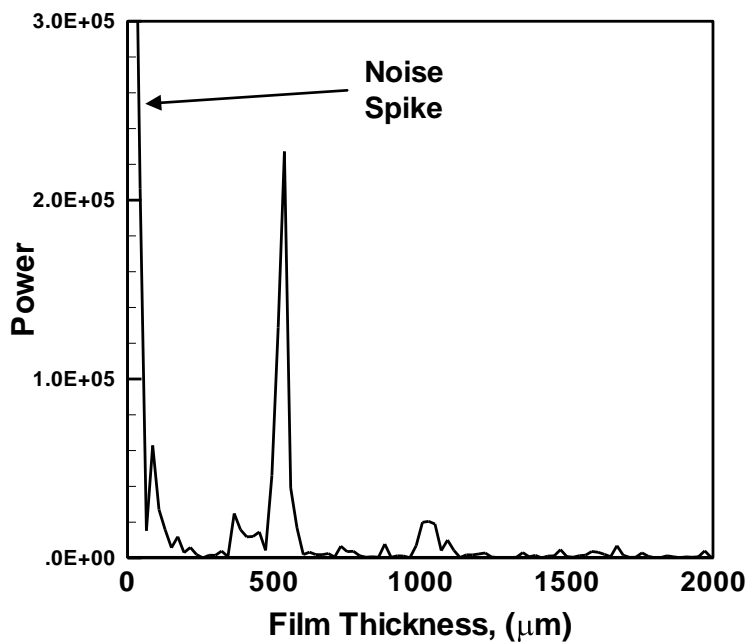


Figure 14. Results of FFT showing the low-end noise spike near zero.

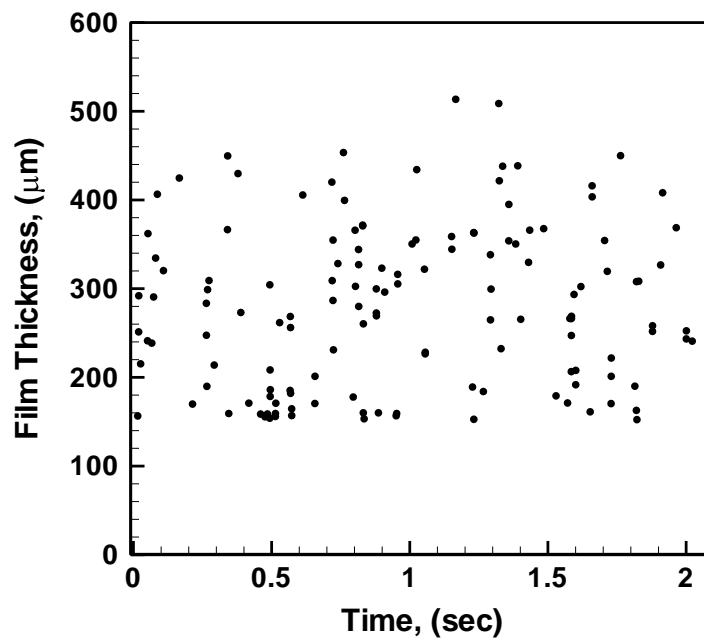


Figure 15. Time series of thickness measurement results for 30 m/s gas phase velocity and $13.01 \text{ cm}^3/\text{s}$ liquid flow rate.

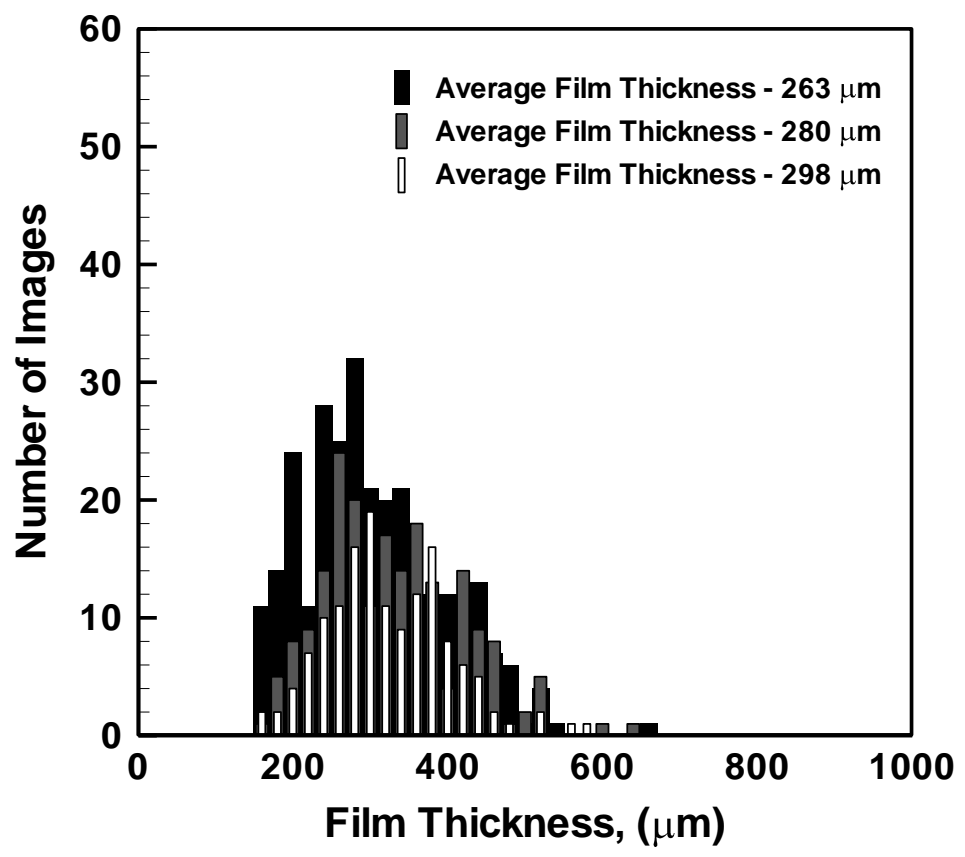


Figure 16. Distribution of film thickness measurements for three tests at 30 m/s gas velocity and 13.01 cm³/s liquid flow rate.

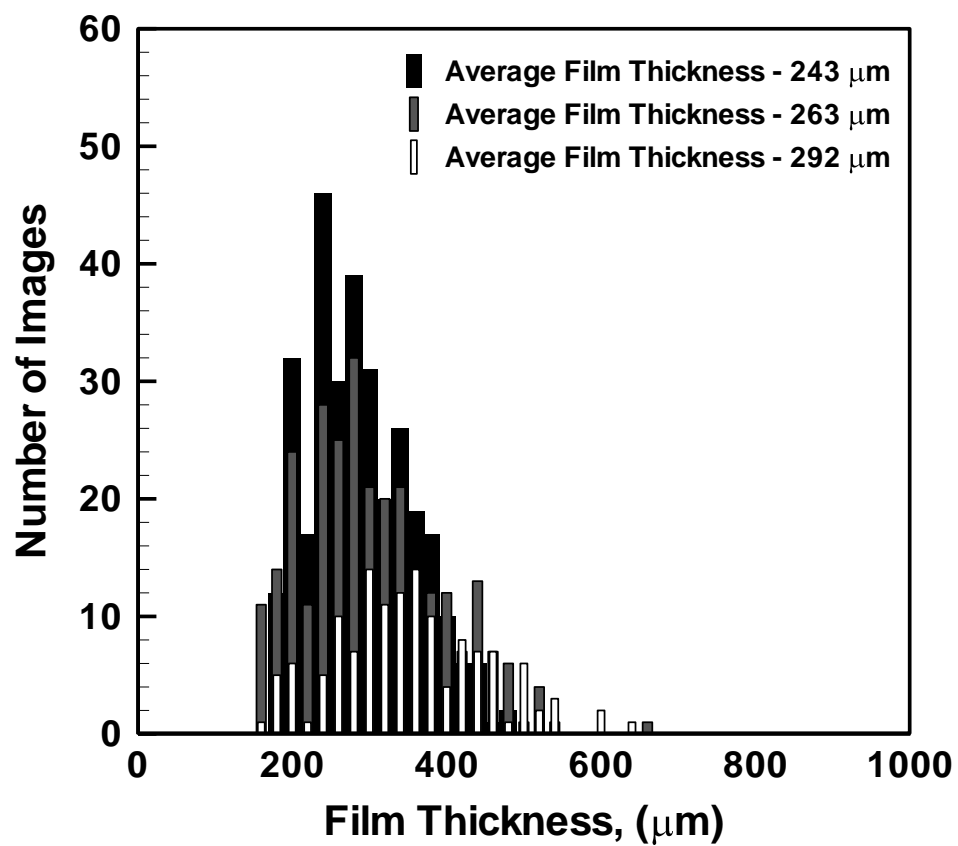


Figure 17. Distribution of film thickness measurements for tests at 30 m/s gas velocity and 6.46, 13.01, and 16.34 cm^3/s liquid flow rates respectively.

Nomenclature

F = number of fringes in the interference pattern

t = film thickness

n_g = index of refraction of gas

n_l = index of refraction of liquid film

β = angle of refraction (measured from the normal to the film)

δ = phase difference of the light reflected off of the top and bottom surfaces of the film

λ_0 = wavelength of incident light

θ_i = incidence angle

m/s = meters per second

mm = millimeter

μm = micrometer

cm^3/s = cubic centimeters per second

\dot{V}_f = film volumetric flow rate

w_f = film width

References

- [1] J. Klausner, L. Zeng and D. Bernhard, Development of a Film Thickness Probe Using Capacitance for Asymmetrical Two-phase Flow with Heat Addition, *Rev Sci Instrum*, vol. 63, pp. 3147-3152, 1992.
- [2] M. Suyar and A.H. Lefebvre, Film Thickness Measurements in a Simplex Swirl Atomizer, *J Propulsion*, vol. 2, pp. 528-533, 1986.
- [3] A. Schagen and M. Modigell, Local Film Thickness and Temperature Distribution Measurement in Wavy Liquid Films with Laser-induced Luminescence Technique, *Exp Fluids*, vol. 43, pp. 209-221, 2007.
- [4] F. Maroteaux, D. Llory, J.F. le Coz and C. Habchi, Potential of Inertial Instabilities for Fuel Film Separation in Port Fuel Injection Engine Conditions, *Int J Engine Res*, vol. 4, pp. 11-26, 2003.
- [5] J. Yang and L.A. Melton, Fluorescence-based Method Designed for Quantitative Measurement of Fuel Film Thickness During Cold-start Engines, *Appl Spectrosc*, vol. 54, pp. 565-574, 2000.
- [6] D.I. Driscoll, R.L. Schmitt and W.H. Stevenson. Thin Flowing Liquid Film Thickness Measurement by Laser Induced Fluorescence, *J Fluids Eng*, vol. 114, pp. 107-112, 1992.
- [7] B.T. Shaw II, D.P. Hault and W. Wong, Development of Engine Lubricant Film Thickness Diagnostics Using Fiber Optics and Laser Fluorescence, *International Congress and Exposition*, SAE Paper 920651, Detroit, 1992.
- [8] L.L. Ting, Development of a Laser Fluorescence Technique for Measuring Piston Ring Oil Film Thickness, *J Lubr Technol*, vol. 102, pp. 165-171, 1980.
- [9] A.A. Mouza, N.A. Vlachos, S.V. Paras and A.J. Karabelas, Measurement of Liquid Film Thickness Using a Laser Light Absorption Method, *Exp Fluids*, vol. 28, pp. 355-359, 2000.
- [10] J.D. Barter, K.L. Beach and P.H.Y. Lee, Collocated and Simultaneous Measurement of Surface Slope and Amplitude of Water Waves, *Rev Sci Instrum*, vol. 64, pp. 2661-2665, 1993.
- [11] J.D. Barter and P.H.Y. Lee, Real-time Wave-amplitude Spectrum Analyzer for Air-liquid Interfaces, *Appl Phys Lett*, vol. 64, pp. 1896-1898, 1994.
- [12] S. Wittig, J. Himmelsbach, B. Noll, H.J. Feld and W. Samenfink, Motion and Evaporation of Shear-driven Liquid Films in Turbulent Gases, *J Eng Gas Turbine Power*, vol. 114, pp. 395-400, 1992.

- [13] E.T. Hurlburt and T.A. Newell, Optical Measurement of Liquid Film Thickness and Wave Velocity in Liquid Film Flows, *Exp Fluids*, vol. 21, pp. 357-362, 1996.
- [14] T.A. Shedd and T.A. Newell, Automated Optical Liquid Film Thickness Measurement Method, *Rev Sci Instrum*, vol. 69, pp. 4205-4213, 1998.
- [15] R. Roy, J. Ku, I. Kaufman and J. Shukla, Microwave Method for Measurement of Liquid Film Thickness in Gas-liquid Flow, *Rev Sci Instrum*, vol. 57, pp. 952-956, 1986.
- [16] T. Takamasa and T. Hazuku, Measuring Interfacial Waves on Film Flowing Down a Vertical Plate Wall in the Entry Region Using Laser Focus Displacement Meters, *Int J Heat Mass Trans*, vol. 43, pp. 2807-2819, 2000.
- [17] T. Ohyama, K. Endoh, M. Atsushi and Y.H. Mori, Optical Interferometry for Measuring Instantaneous Thickness of Transparent Solid and Liquid Films, *Rev Sci Instrum*, vol. 59, pp. 2018-2022, 1988.
- [18] T. Nosoko, Y.H. Mori and T. Nagata, Improved Interferometer for Measuring Unsteady Film Thickness, *Rev Sci Instrum*, vol. 67, pp. 2685-2690, 1996.
- [19] P. Kelly-Zion, W. Collins and D. Glawe, Application of Laser Interferometry for Transient Film Thickness Measurements, *Proceedings of 2004 ASME Heat Transfer/Fluids Engineering Summer Conference*, Charlotte, 2004.
- [20] M. Friedrich, H. Lan, J. Wegener, J. Drallmeier and B. Armaly, A Separation Criterion with Experimental Validation for Shear-driven Films in Separated Flows, Accepted for publication in *J Fluids Eng*, 2008.
- [21] H. Lan, M. Friedrich, B. Armaly and J. Drallmeier, Simulation and Measurement of 3D Shear-driven Thin Liquid Film Flow in a Duct, *Int J Heat and Fluid Flow*, vol. 29, pp. 449-459, 2008.

3. CONCLUSIONS

An experimental test facility to study the development of a shear-driven liquid film and its subsequent separation at an expanding corner has been developed. Built into the test section is the ability to measure the liquid mass which stays attached to the wall after the corner. An analytical force balance was developed to serve as a prediction of the onset of film separation. Required for the force balance is knowledge of the film thickness and velocity at the corner, which were determined using a simple rough wall film propagation model for demonstration purposes.

The force balance of the major liquid phase forces acting at the corner, including surface tension, film inertia, and gravity, correlated well to the onset of film separation as measured in the experiment. Effects of the wall angle on film separation are included, unlike previous Weber number models. Additionally, the mass fraction of the liquid film which separates from the wall correlates to the Force Ratio over a wide range of experimental test conditions. The correlation of the separated mass to the liquid film force balance suggests the gas phase impacts the separation process only through its effect on the liquid film momentum. It is surmised, however, the inclusion of gas phase effects in the shear layer and recirculation zone will be necessary to consider the breakup of the film.

An optical interferometric film thickness measurement system was also discussed for use in measuring the mean film thickness of dynamic, shear-driven thin liquid films with surface instabilities. The experimental test facility was modified to allow access to obtain film thickness measurements using this technique. Validation of the optical system was performed using a droplet of water of known volume, as well as a sapphire

disk, obtaining results within the manufacturer's uncertainty of 10%. Optimization of the optical system for use with dynamic films was also discussed.

Automatic identification and subsequent analysis of interference patterns in the captured images was performed using a Fast Fourier Transform approach, which makes use of the concept that one, single unique frequency exists in an image with a discernable fringe pattern, corresponding to the film thickness at that instant. An automated algorithm for identification of images with a pattern and the subsequent determination of the film thickness has been developed and demonstrated. Important considerations for accurate measurement of the film thickness were discussed along with experimental results showing the capability of the technique to capture the average thickness of the shear-driven film.

APPENDIX A.

EXPERIMENTAL SETUP – TEST SECTION AND MEASUREMENT SYSTEMS

The details of the experimental equipment used, as well as the procedures for establishing each flow condition, are given in Appendix A. The flow facility used in this experiment was developed in order to study shear-driven liquid film propagation and the ensuing separation and break-up at a sharp expanding corner. The flow system consists of a four part test section mounted to an optics table platform. Flow is pulled through the test section using a large liquid ring vacuum pump and flow rates through the test section are determined using a laminar flow element with a GE Druck LP1810-C1SNW-1 differential pressure sensor with a range of 0-10 inches of water. Corrections are made for local temperatures and pressures resulting in uncertainties of less than 3% in the measured gas flow rate.

A schematic of the test section is shown in Figure 1. A 1.43 m long entrance region (not shown) provides for two-dimensional flow span-wise across the test section at the point of film introduction. The dimensions of the test section at the point of film introduction and up to the corner are 2 cm tall by 10 cm wide, giving an aspect ratio of 5. The liquid is introduced through a porous brass plug on the bottom wall in the film introduction section. The plug is not across the entire span of the section, but is over the center 7.5 cm width of the test section to negate three-dimensional effects. The liquid flow into the test section is provided by a two gallon pressurized stainless steel tank with an ASCO 8262C86E solenoid valve to start and stop the flow. Flow rate is quantified on a volumetric flow basis and measured using an Omega FL-3663ST rotometer for the lower flow rates and an Omega FL-2051 rotometer for the high flow rates. For the results presented here, the liquid was water with the addition of a surfactant (Surfynol 465) at 0.1% and 1.0% by mass which results in a surface tension, σ , of 0.042 N/m and

0.026 N/m, respectively. The surfactant had minimal effect on the fluid viscosity which was measured to be 0.983×10^{-3} Ns/m² for the 0.1% solution and 1.027×10^{-3} Ns/m² for the 1.0% solution, effectively the same as water at ambient conditions.

The corner section is removable from the configuration such that the angle of the corner in the bottom wall may be changed. For all experiments shown here a 60° angle, measured from the horizontal, was used. Optical access is provided from the top, 40mm upstream and 40mm downstream of the corner, to enable measurement of an average film thickness. The film thickness measurement was made on the centerline, 5 mm in front of the corner, so that the corner had negligible effect on the liquid film flow. The length of the duct from the point of film introduction to the corner is 23 cm. After the corner, the duct has an aspect ratio of 1.429 wherein an exit section provides for a transition from the test section to the 10.2 cm diameter piping which runs to the liquid ring pump. A Starett high-precision level was used to ensure the test section was horizontal to prevent biasing of the film flow.

Significant effort was expended in developing a test section which resulted in uniform gas phase velocities span-wise across the test section near the corner. Although the film is introduced uniformly over the center 7.5 cm width of the test section, the film width changes as it reaches the corner due to surface tension. Therefore, the film width is measured based on imaging through a window in the top of the test section with an uncertainty of 3 % determined by parallax and scale resolution.

High Speed Imaging System

The general characteristics of the liquid film, including the surface instabilities and interaction of the film with the separated gas phase at the corner, were characterized

using high speed imaging. A Photron 1280 PCI high speed camera, with close-up lenses totaling +7 diopter, was used to capture 2000 frames per second at 640 X 256 resolution. The backlighting for the shadowgraph image was accomplished by shining a Solarc Light light source through a diffuser (notebook divider from Staples) and then reflecting the diffused light 90 degrees into the test section using a parabolic mirror with a focal length of 11.35 inches.

Optical Hardware Configuration for Film Thickness Measurement

The optical configuration of the film thickness measurement system is shown in Figure 2. A 10 mW HeNe laser is collimated using several Spindler & Hoyer / Linos lenses to approximately a 20 mm diameter. A 100 mm focal length lens is used at the end of the transmitting optics to develop a spot size of less than 0.01 mm diameter on the film.

The light reflected from the film, which forms the interference pattern, is imaged on an image target. In the study by Kelly-Zion et al. (35) frosted glass was used as the image target, however, due to the finish on the frosted glass, the resolution of the fringe pattern captured with the high-speed camera was less than ideal for image post-processing because of the presence of random bright pixels within the image. Therefore, in order to improve the image quality for post-processing a neutral density filter was used in this study as the image target. The field of view was defined by the aperture used in the receiving optics. Temporal resolution was determined by the rate at which the imaging took place. For the results shown here, a high frame-rate camera, a Photron 1280 PCI, was used operating at 4000 frames per second.

The parameters affecting image quality include the camera aperture setting, camera shutter speed, and sensitivity. The camera aperture setting and shutter speed are intimately related as observed during the testing. Therefore, changing one required changing the other in order to obtain a good quality image. The image quality was determined by a visual inspection of the fringe patterns, looking for fringe clarity, contrast, and intensity. The optimal settings were chosen to maximize contrast with a shutter speed of 1/4000 second and can be found in Appendix D.

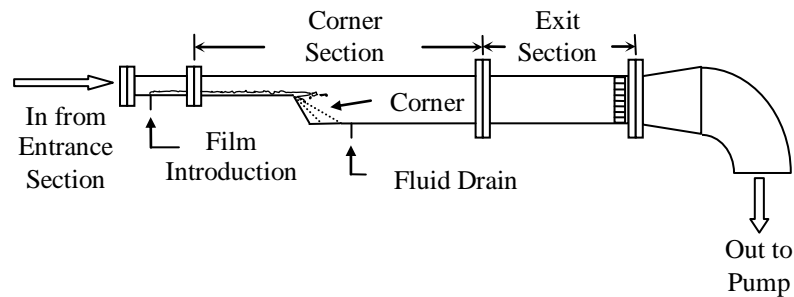


Figure 1. Schematic of experimental test section.

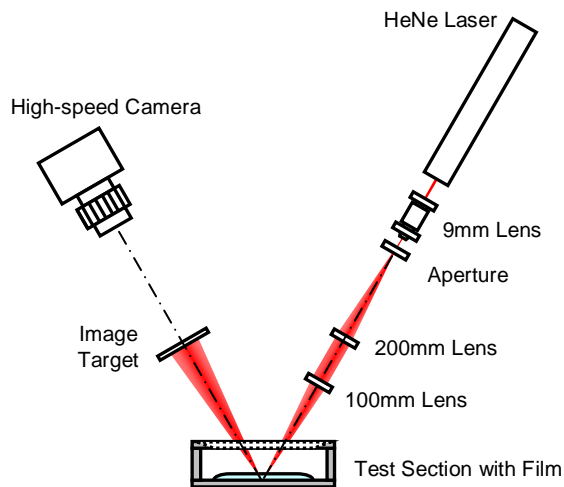


Figure 2. Schematic of the optical system for the interferometric film thickness measurement.

APPENDIX B.

FILM SEPARATION ANALYSIS DATA COLLECTION PROCEDURE

The details for the data collection procedures for the film separation analysis are given in Appendix B. The data collection process to measure the amount of film separation at the corner involved a simple system designed to extract the liquid which stayed attached to the downward sloping wall after the corner. As shown in Figure 3, a porous brass plug was placed downstream of the test section corner on the downward slope of the lower wall to serve as a means to remove the mass of the liquid film that remained attached to the wall. The porous plug (6 mm wide) extends across the span of the test section and was placed flush with the sloping wall to prevent any disturbance of the flow. The brass plug is located 6 mm down the wall from the corner, which was determined by high speed imaging flow visualization to be far enough downstream from the corner as to not impact the film separation process and yet upstream from liquid which may be pulled up the sloping wall by the recirculation flow region behind the step.

After the flow reached a steady state condition, suction was applied below the porous plug with a Thomas vacuum pump to remove the liquid from the wall. Sufficient suction was applied behind the porous plug, adjusted at each flow condition, for complete removal of the liquid from the wall while pulling the minimum amount of gas through the porous surface. The liquid was captured in a polypropylene bottle and the mass was measured using a mass balance with a resolution of ± 0.1 gram. High speed imaging was used initially at each set point to ensure all of the liquid film was removed from the wall. Liquid film collection times were measured using a stopwatch and were on the order of 1 minute in duration with an uncertainty of $\sim 1\%$. A determination of the mass flow of liquid attached to the wall was made by dividing the captured mass of liquid by the time, which, when subtracted from the measured liquid flow rate into the test section, provided

the mass flow of liquid separated at the corner. Combined uncertainty in this measurement was 5 %.

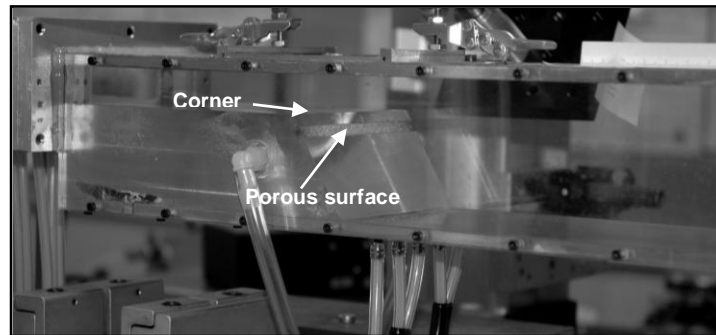


Figure 3. Picture of test section showing porous surface where film which remains attached after the corner is removed.

APPENDIX C.

FILM THICKNESS MEASUREMENT DATA REDUCTION PROCEDURE

The details for the data reduction processes used for the analysis of the film thickness measurement data are given in Appendix C. Figure 4 shows the image identification and analysis protocol in a block diagram format. This algorithm is applied to an entire set of images captured for a specific flow condition and the output to the user is a plot and list of a time series of film thickness values for the set. This set can then be used to determine an average film thickness for the specific flow condition. Inputs to the algorithm include the crop size (measured in pixels) for the corresponding aperture used, FFT low end noise spike cutoff value, column averaging width, FFT signal to noise ratio, and the percent of columns with a pattern required for an image to be considered valid. A commented printout of the MATLAB program developed for this task is shown below

```

% FFT analysis of fringe spacing in bitmap files
% Program created July 2006
% For use with NSF thin-film project
% Version 4.1
% last modified 3/26/07
% uses FFT Power Method of data analysis, as opposed to common
magnitude
% method of interpretation for FFT raw output data
%
% new approach in version 3
% combining pixel intensities prior to FFT analysis
% then signal to noise corrections
%
% adjust for each image set:
% 1) image cropping and parameters in first form
% 2) optics parameters in second form
%
% 3b2 moved to histogram analysis, counting bin count within three of
peak
% input then taken from first dialog box as to required value
%
% 3b3 input in dlg prompt changed to std dev max off arrValidPeak
instead
% of counting values in bins to left or right of peak bin
% bin counting code retained for comparison, not deleted
%
% 4: fixed error with low end FFT noise by altering origin of input
signal
% fixed fft point error
%
% 4.1 revolution edition
% normalization of pixel values pre-FFT input about average for a given
% blurred column, like audio signal normalized about zero
% should show +/- oscillations about netraul color of choice

%Importing of bitmap files into three-dimensional array
clear
bmpList = dir('*.*bmp');
filedim = numel(bmpList);

%Trim image to aperature size
prompt={'Top, left coordinate of crop (x)', 'Top, left coordinate of
crop (y)', 'Bottom, right coordinate of crop (x)', 'Bottom, right
coordinate of crop (y)', 'lower peak cutoff', 'upper peak cutoff', 'StdDev
Multiplier', 'col width (pix)', 'valid peak %', 'avg FFT s/n'};
dlg_title='Aperature window crop coordinates';
num_lines=1;
%255x640, 420 exposed, first image sets
%def={'1', '118', '256', '538', '0.065', '0.30', '4.5', '5', '20', '5'};
%new images as of 1-19 - 410 pixels / 11.75 mm
%255x640, 410 exposed
%def={'1', '53', '128', '464', '0.1', '0.50', '4.5', '3', '15', '12'};
%128x640 images, 18 blank on top, 17 blank on bottom
def={'1', '59', '128', '584', '0.05', '0.37', '5', '5', '25', '10'};
cropdata=inputdlg(prompt,dlg_title,num_lines,def);
cropdata=str2double(cropdata);
x1=cropdata(1);

```

```

y1=cropdata(2);
x2=cropdata(3);
y2=cropdata(4);
floorCrop=cropdata(5);
ceilCrop=cropdata(6);
dblSigmaMult=cropdata(7);
xcolwidth=cropdata(8);
dblValidPeakPerc=cropdata(9)/100;
dblSN=cropdata(10);
xdist=x2-x1;
ydist=y2-y1;
fftPoint=ydist;
fprintf('width of aperature input (pixels): %.0f\n',xdist);
fprintf('height of aperature input (pixels): %.0f\n',ydist);
%End trim image aperature size

%Film thickness calculation from fft data result
prompt={'wavelength \lambda (mm)', '\beta 1 (deg)', '\beta 2 (deg)', 'film
parameter n', 'liquid phase flow (mm)'};
dlg_title='Film Thickness Calculation Input Parameters';
num_lines=1;
%def={'6.33e-4', '15.59358', '17.287884', '1.766', '20'}; %sapphire
%def={'6.33e-4', '20.926448', '23.228754', '1.33', '20'}; %water
%def={'6.33e-4', '17.71427965', '20.64638587', '1.521', '20'}; %Slide
cover
def={'6.33e-4', '20.36298547', '23.7806206', '1.33', '30'}; %new
water
filmdata=inputdlg(prompt,dlg_title,num_lines,def);
filmdata=str2double(filmdata);
lambda=filmdata(1);
beta1=filmdata(2);
beta2=filmdata(3);
fpn=filmdata(4);
liquidflow=filmdata(5);
%Finding peak of data for one single image, cutting off lower % of fft
%result data

dblPeakIndex = 0;
dblBinWide = 50;
%Bin width for histogram
%Begin image processing into individual arrFFTin, then fft analysis

waitFFT = waitbar(0, 'Acquiring / Performing FFT');
for fc=1:filedim %main file processing loop
    %begin transplant file acquisition on singular basis
    rawIMG = imread(bmpList(fc).name, 'bmp');
    imgfile = bmpList(fc).name;
    fprintf('%.0f: ',fc);
    fprintf('file read: %s\n',imgfile);
    arrIMG = double(rawIMG);
    clear rawIMG

    %image crop
    xstep = 0;
    ystep = 0;
    for j=y1:(y2-1)
        ystep = ystep + 1;

```

```

        xstep = 0;
        for i=x1:(x2-1)
            xstep = xstep + 1;
            arrIMGcrop(ystep,xstep) = arrIMG(j,i);
        end
    end
%end image crop
xdim = xdist;
ydim = fftPoint/2;
xcolumn = floor(xdist/xcolwidth);
xstep = 0;
ystep = 0;
xcolstep = 1;
xcolchange = 0;
arrColSum = zeros(ydist,xcolumn);
%pixel blurring loop
%renders new FFT input file with column averages

%adds, averages pixel values, blurring
for xstep=1:(xcolumn*xcolwidth)
    xcolchange = xcolchange + 1;
    for ystep=1:ydist
        arrColSum(ystep,xcolstep) = arrColSum(ystep,xcolstep) +
arrIMGcrop(ystep,xstep);
        end
        if xcolchange == xcolwidth
            xcolstep = xcolstep + 1;
            xcolchange = 0;
        end
    end
end
if fc == 1
    fprintf('    width of aperature processed (pixels):
%.0f\n',xstep);
    fprintf('    height of aperature processed (pixels):
%.0f\n',ystep);
end
arrFFTin = arrColSum/xcolwidth;
%/blurring pixel values

%for ystep=1:ydist
%    arrIMGwrite(ystep,fc) = arrFFTin(ystep,20);
%end
%writing out edited image to file

%xcolstep = 1;
%xcolchange = 0;

%for xstep=1:(xcolumn*xcolwidth)
%    xcolchange = xcolchange + 1;
%    for ystep=1:ydist
%        arrIMGwrite(ystep,xstep) = arrColAvg(ystep,xcolstep);
%    end
%    if xcolchange == xcolwidth
%        xcolstep = xcolstep + 1;
%        xcolchange = 0;
%    end
%end

```

```

%imwrite(arrIMGwrite,bmpList(fc).name,'bmp');

%4.1 revolution
%normalization of pixel values about mean for given column
for xcolstep=1:xcolumn
    arrFFTin(:,xcolstep) = arrFFTin(:,xcolstep) -
mean(arrFFTin(:,xcolumn));
end
%/4.1 revolution mods

%now that the blurred pixel matrix is created, FFT is performed on
all
%columns - array size not same as original image
arrFFToutraw = fft(arrFFTin,fftPoint);
%magnitude method and power method fft selection area
%arrFFToutraw = abs(arrFFToutraw);
%magnitude method
arrFFToutraw = arrFFToutraw.* conj(arrFFToutraw) / fftPoint;
%power method, best
%/end fft method selection

xstep = 0;
ystep = 0;
xcolstep = 0;
xcol = 1;
dblValidPeak = 0;
dblHistBinCount = 0;
dblHistBinCountCheck = 0;

if fc == 1;
    fcrop = floor(ydim*floorCrop); % cuts lower off
    %if fcrop < 1
    %    fcrop = 1;
    %end
    fceil = floor(ydim*ceilCrop); % ceiling on peak window search
    frange = fceil - fcrop;
    arrFFTplot=zeros(frange,1);
    arrFFTplot(1) = fcrop; %seed floor value for plotting array
    for i = 2:frange
        arrFFTplot(i) = arrFFTplot(i-1) + 1;
    end
    arrFFTplot = ydist*arrFFTplot/fftPoint;
    arrFFTplot = ((lambda*arrFFTplot)/(2*fpn*(cosd(beta1) -
cosd(beta2)))) * 1000;
    dblBinCount = ceil(arrFFTplot(frange-fcrop)/dblBinWide);
    arrHistPeak(:,1) = arrFFTplot(1):(arrFFTplot(frange)-
arrFFTplot(1))/dblBinCount:arrFFTplot(frange);
end

%cut arrFFTout to concerned window for easier processing in later
sec
for xcolstep=1:xcolumn
    for cropstep=1:frange
        arrFFTout(cropstep,xcolstep) =
arrFFToutraw(((fcrop)+cropstep),xcolstep);
    end
end
end

```

```

arrStdDev = std(arrFFTout);
arrFFTmean = mean(arrFFTout);

%finding valid peaks
arrFFTpeak=zeros(xcolumn,2);
    %column 1 is fft point location of peak
    %column 2 is value of peak
for xcolstep=1:1:xcolumn
    for fftstep=1:frange %steps across FFT and finds peak
        if arrFFTpeak(xcolstep,2) <= arrFFTout(fftstep,xcolstep) &&
arrFFTout(fftstep,xcolstep) > 100 %for black images
            arrFFTpeak(xcolstep,1) = fftstep + fcrop;
            arrFFTpeak(xcolstep,2) = arrFFTout(fftstep,xcolstep);
        end
    end
    %determines if valid peak above StdDev cutoff
    if arrFFTpeak(xcolstep,2) > arrFFTmean(xcolstep) +
dblSigmaMult*arrStdDev(xcolstep)
        dblValidPeak = dblValidPeak + 1;
        arrValidPeak(dblValidPeak,1) = xcolstep; %column of valid
peak
        arrValidPeak(dblValidPeak,2) = arrFFTpeak(xcolstep,1); %x
axes fft point loc
        arrFilterFFT(:,dblValidPeak) = arrFFTout(:,xcolstep); %FFT
of valid peak curves
    end
end
%conversion of x axes fft point to thickness in um
if exist('arrValidPeak','var') ~= 0
    arrValidPeak(:,2) = ydist*arrValidPeak(:,2)/fftPoint;
    arrValidPeak(:,2) =
((lambda*arrValidPeak(:,2))/(2*fpn*(cosd(beta1) - cosd(beta2)))) *
1000;

%histogram creation
arrHistPeak(:,2) = 0;
arrHistPeak(:,2) = histc(arrValidPeak(:,2),arrHistPeak(:,1));
%use histogram to find peak for results array
%find histogram peak, get result thickness from average of 2
surr bins
for binstep=1:1:(dblBinCount+1)
    if arrHistPeak(binstep,2) == max(arrHistPeak(:,2));
        if binstep == 1 % peak on low end of hist
            arrHistAvgWindow(1) = arrHistPeak(1,1);
            arrHistAvgWindow(2) = arrHistPeak(3,1);
        elseif binstep == (dblBinCount+1) % peak on top end of
hist
            arrHistAvgWindow(1) = arrHistPeak(dblBinCount,1);
            arrHistAvgWindow(2) = arrHistPeak(dblBinCount+1,1);
        else % peak in middle of hist
            arrHistAvgWindow(1) = arrHistPeak(binstep-1,1);
            arrHistAvgWindow(2) = arrHistPeak(binstep+1,1);
        end
    end
end
end
%histogram representation into bins from good std determined
columns

```

```

        if (dblValidPeak >= (dblValidPeakPerc*xcolumn)) &&
((mean(arrFFTpeak(:,2))/mean(arrFFTmean)) >= dblSN)
            dblPeakIndex = dblPeakIndex + 1;
            arrResults(dblPeakIndex,1) = fc; %image file location of
comp
            arrResults(dblPeakIndex,2) = 0; %seed for histogram peak
calc
            for peakstep=1:dblValidPeak
                if (arrValidPeak(peakstep,2) >= arrHistAvgWindow(1)) &&
(arrValidPeak(peakstep,2) < arrHistAvgWindow(2))
                    dblHistBinCount = dblHistBinCount + 1;
                    arrResults(dblPeakIndex,2) =
arrResults(dblPeakIndex,2) + arrValidPeak(peakstep,2);
                    %arrValidPeaks valid from each column within hist
window
                    %are averaged for result thickness of image result
                end
            end
            arrResults(dblPeakIndex,2) = arrResults(dblPeakIndex,2) /
dblHistBinCount; %final result thickness
            arrResults(dblPeakIndex,3) = std(arrValidPeak(:,2)); %std
dev of valid point array values
            arrResults(dblPeakIndex,4) =
mean(arrFFTpeak(:,2))/mean(arrFFTmean); %Sig/noise avg for image
        else
            dblPeakIndex = dblPeakIndex + 1;
            arrResults(dblPeakIndex,1) = fc;
            arrResults(dblPeakIndex,2) = 0;
            arrResults(dblPeakIndex,3) = 0;
        end
    else
        dblPeakIndex = dblPeakIndex + 1;
        arrResults(dblPeakIndex,1) = fc;
        arrResults(dblPeakIndex,2) = 0;
        arrResults(dblPeakIndex,3) = 0;
    end
clear arrIMG
clear arrFFTmean
clear arrFFTpeak
if fc ~= filedim
    clear arrValidPeak
    clear arrFFTin
end
    %clear arrValidPeak because if less xcolumn than image before,
    %higher numbered columns will still override and mess hist up
    waitbar(fc/filedim)
end %main file processing loop
close(waitFFT);

%Plotting section

%Plotting of results
fftPlot=fftPoint/2;

%v3 - plotting FFT of image columns
%if filedim == 1

```

```
figure('Name','FFT of blurred pixel columns from last image in
set')
plot(arrFFTplot,arrFFTout)
title({'Band Frequency Average - ',num2str(fftPoint),' point
FFT'};['File name: ',imgfile,' Columns: ',num2str(xcolumn),''])
xlabel('film thickness (\mum)')
%end
arrTime=[2
12
39
47
67
76
83
135
146
165
166
167
175
176
183
184
186
188
189
190
192
206
209
210
219
222
226
241
242
256
268
280
284
285
292
293
300
362
366
372
376
377
386
387
420
428
466
478
482
483
```



```

486
508
509
518
519
520
562
570];
arrTime=(arrTime/2000)*1000;
if exist('arrResults','var') ~= 0
    figure('Name','Thickness vs. Image Frame')
    plot(arrResults(:,1),arrResults(:,2));
    title(['Film Thickness vs. image frame - ',num2str(liquidflow),'mm
liquid flow'];['lower FFT cutoff (LH only) -
',num2str(floorCrop*100),'%', upper FFT cutoff -
',num2str(ceilCrop*100),'%'];['peak cutoff - ',num2str(dblSigmaMult),'x
std dev above mean, ',num2str(dblPeakIndex),' of ',num2str(filedim),'
images']]})
    xlabel('time (ms)')
    ylabel('film thickness \mum')
end
if (exist('arrHistPeak','var') ~= 0) && (exist('arrValidPeak','var') ~=
0) %&& (filedim == 1)
    figure('Name','Histogram of valid peak thickness values')
    bar(arrHistPeak(:,1),arrHistPeak(:,2))
    title(['Histogram of valid peak thickness values -
',num2str(liquidflow),'mm liquid flow'];['lower FFT cutoff (LH only) -
',num2str(floorCrop*100),'%', upper FFT cutoff -
',num2str(ceilCrop*100),'%'];['peak cutoff - ',num2str(dblSigmaMult),'x
std dev above mean, ',num2str(dblPeakIndex),' of ',num2str(filedim),'
images']]})
    xlabel('film thickness \mum')
    ylabel('count')
end

%Plotting of FFT results, for each image in series
dblCropThicknessLow = arrFFTplot(1);
dblCropThicknessHigh = arrFFTplot(fceil - fcrop);
dblThicknessRes = 1; %unit step for thickness against fft point used
dblThicknessRes = ydist*dblThicknessRes/fftPoint;
dblThicknessRes = ((lambda*dblThicknessRes)/(2*fpn*(cosd(beta1) -
cosd(beta2)))) * 1000;
fprintf('lower peak window cutoff (um): %.1f\n',dblCropThicknessLow);
fprintf('upper peak window cutoff (um): %.1f\n',dblCropThicknessHigh);
fprintf('max step resolution (um); %.2f\n',dblThicknessRes);
fprintf('actual histogram columb width (um);
%.3f\n\n', ((arrFFTplot(frange)-arrFFTplot(1))/dblBinCount));

```

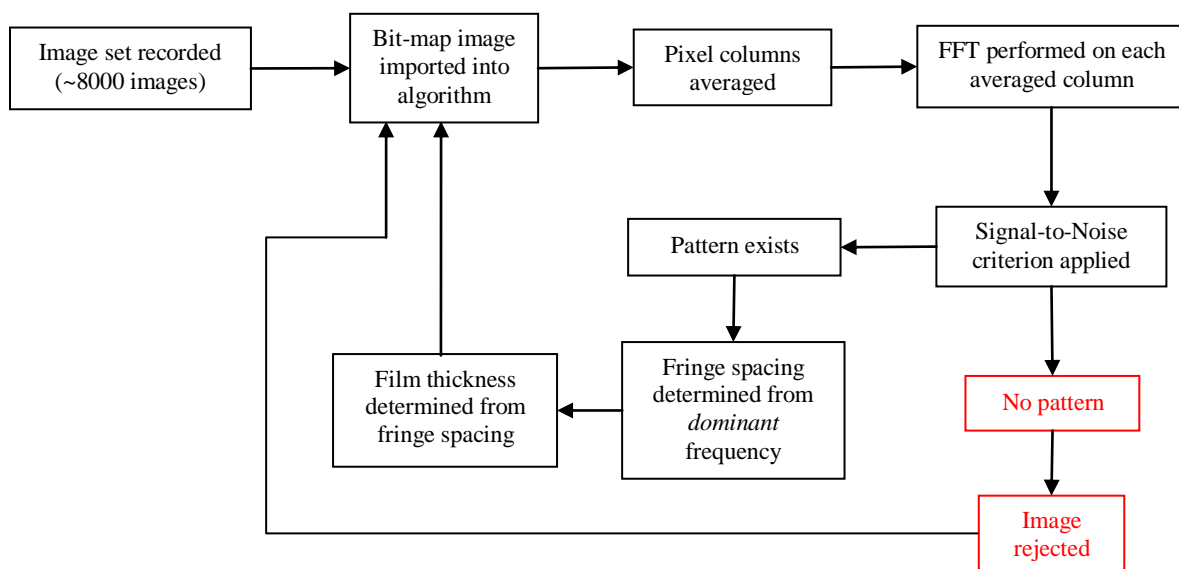


Figure 4. Block diagram of image identification and analysis protocol.

APPENDIX D.

FILM THICKNESS MEASUREMENT TECHNIQUE

LASER ORIENTATION TESTING

The details of the laser orientation testing and setup are given in Appendix D. The first step in determining the optimum settings for the film thickness measurement technique was to list the possible parameters that affect the measurement, and to determine which of those parameters could be varied to obtain the optimal setting. The following were selected as possible parameters that could be adjusted in order to obtain these settings:

1. Laser incident and receiving angles - 30° or 45°.
2. Camera Aperture setting.
3. Camera shutter speed – determined by software
4. Sensitivity
5. Gamma

From the theoretical calculations of spot size on the film, it was determined that the 100mm focal length lens resulted in a spot size approximately one half the diameter of the 200mm focal length lens. Therefore the 100mm lens was used for all cases in order to optimize the spatial resolution of the measurement. The distance from the receiving screen to the film was not varied in this experiment because the previous location of the screen was determined to be appropriate based on the aperture sizing and the fringe spacing in the images. One other note, the camera aperture setting and shutter speed are intimately related as observed during the testing, therefore, changing one required changing the other in order to obtain a good quality image.

In order to determine the optimal setting for each parameter, a test matrix was composed such that all parameters could be analyzed simultaneously. It was determined that each test case would be run and then the first 250 images of each case would be analyzed to determine the presence or absence of fringes. Table 1 shows this test matrix

and the results obtained from the analysis for the 30 degree orientation, and Table 2 shows the same for the 45 degree orientation.

The images were analyzed by grouping them according to the sensitivity and looking at several cases at a time. The notes acquired during this image analysis were as follows:

30 deg Orientation:

Runs 1-4: Images do not have any clear fringes even when fringes appear. Difficult to determine background noise from fringe pattern. Many black/white images. Lot of background noise.

Runs 5-8: Fewer black/white images than x8 sensitivity, but still quite a few. Fringes seem clearer than x8 sensitivity, but still have background noise.

Runs 9-10: More background noise than 45 degree orientation, but fringe patterns are more easily discernable. Not as much background noise as 2.0 aperture.

45 deg Orientation:

Runs 1-4: Many black images. Fringes are not clear even when they appear.

Runs 5-8: Lot of background noise. Fringes not clear even when they appear. Many black/white images.

Runs 9-10: Many black images. Pretty good image if fringes appear. (Frame 159)

As is evident from the results, the 30 degree orientation resulted in more discernable images than the 45 degree orientation, and the 1.6 aperture setting resulted in the greatest number of discernable images among the 30 degree orientation settings. Therefore the following optimal settings were chosen for the parameters associated with this measurement technique:

1. Laser light incident and receiving angles - 30°
2. Camera aperture setting - 1.6
3. Camera shutter speed - $1/4000$ sec
4. Sensitivity - x8
5. Gamma - 1.0
6. Focusing lens - f#100

Table 1. 30 Degree Orientation Test Matrix and Results

8/2/2006 - Laser Orientation Testing - f#100 - 30 degrees					
Run #	Aperture	Sensitivity	Gamma	Shutter Speed (sec)	# Discernable Images in 250 frames
1	2.0	x8	0.4	1 / frame rate	5
2	2.0	x8	0.6	1 / frame rate	5
3	2.0	x8	0.8	1 / frame rate	13
4	2.0	x8	1.0	1 / frame rate	9
5	2.0	x4	0.4	1 / frame rate	13
6	2.0	x4	0.6	1 / frame rate	16
7	2.0	x4	0.8	1 / frame rate	19
8	2.0	x4	1.0	1 / frame rate	17
9	1.6	x8	1.0	1 / 4000	36
10	1.6	x4	1.0	1 / 4000	34

Table 2. 45 Degree Orientation Test Matrix and Results

8/3/2006 - Laser Orientation Testing - f#100 - 45 degrees					
Run #	Aperture	Sensitivity	Gamma	Shutter Speed (sec)	# Discernable Images in 250 frames
1	2.0	x4	0.4	1 / frame rate	2
2	2.0	x4	0.6	1 / frame rate	4
3	2.0	x4	0.8	1 / frame rate	5
4	2.0	x4	1.0	1 / frame rate	12
5	2.0	x8	0.4	1 / frame rate	3
6	2.0	x8	0.6	1 / frame rate	3
7	2.0	x8	0.8	1 / frame rate	6
8	2.0	x8	1.0	1 / frame rate	5
9	1.6	x4	1.0	1 / 4000	11
10	1.6	x8	1.0	1 / 4000	9

APPENDIX E.

IMPROVEMENTS TO THE INTERFEROMETRIC FILM THICKNESS

MEASUREMENT TECHNIQUE

Suggestions for improvement to the interferometric film thickness measurement technique are given in Appendix E. Several potential areas of improvement exist for both the optical hardware and the post-processing analysis algorithm, and therefore, an attempt is made here to provide a list of suggested improvements for future investigators. The suggestions are organized into the following categories: optical hardware improvements, experimental improvements, and post-processing algorithm improvements.

Optical Hardware Improvements

High Speed Camera – Though it is probably the most expensive improvement, a higher resolution camera would give a higher resolution of data samples in each column which should improve the FFT analysis and get rid of some of the noise seen in the FFT plot.

Image Target – One of the least expensive and possibly greatest improvements to the optical system would be to use an image target that diffuses the light smoothly, unlike the frosted glass which has random bright and dark spots, or the neutral density filter which allows the Airy rings to be seen. Opal coated glass will give the desired target given that the coating is thin enough, however, all coatings on the glass that was found were too thick, so a special piece may have to be made.

Experimental Improvements

Flow Measurement Hardware – more accurate flow measurement hardware may improve the repeatability of the experimental system to obtain repeatable flow conditions.

Substrate Surfaces – Further experimental testing on a variety of substrate wall surfaces/finishes will help to establish the limits/capability of the system to give reliable results.

Post-processing Algorithm Improvements

Signal to Noise Ratio – The automated algorithm for thickness determination requires further investigation to determine methods to appropriately choose signal to noise criterion based on experimental observations.

FFT Analysis – To reduce the noise spike at low frequency values caused by windowing and quasi-sinusoidal nature of pattern, appropriate data filtering and windowing techniques should be applied. Several of these techniques are available in MATLAB and could be incorporated into the current MATLAB code.

Further investigation into adjusting the dynamic range of the film thickness measurement for specific applications would be very helpful for the end user, so development of a systematic approach to set the dynamic range would be a great improvement to the system.

BIBLIOGRAPHY

1. **Felton, P. G., Kyritsis, D. C. and Fulcher, S. K.** Visualization of Liquid Fuel in the Intake Manifold During Cold Start. *SAE 952464*. s.l. : Society of Automotive Engineers, 1995.
2. **Dawson, M. and Hochgreb, S.** Visualization Using Laser-Induced Fluorescence During Cold Start. *SAE 982466*. s.l. : Society of Automotive Engineers, 1998.
3. **Landsberg, G., Heywood, J. and Cheng, W.** Contribution of Liquid Fuel to Hydrocarbon Emissions in Spark Ignition Engines. *SAE 2001-01-3587*. 2001.
4. **Stanglmaier, R., Li, J. and Matthews, R.** The Effects on In-Cylinder Wall Wetting Location on the HC Emissions from SI Engines. *SAE 1999-01-0502*. 1999.
5. **Hanratty, T. J. and Theofanous (editors), T.** Multiphase Flows: An Assessment With a View to the Future. s.l. : Colloquium, University of Illinois at Urbana-Champaign, November 5-6, 1994.
6. *Wave Evolution on a Falling Film.* **Chang, H. C.** 1994, Annual Review of Fluid Mechanics, Vol. 26, pp. 103-136.
7. *Pressure Driven Disturbances on a Thine Viscous Film.* **Kriegsmann, J. J., Miksis, M. J. and Vanden-Broeck, J. M.** 6, 1998, Physics of Fluids, Vol. 10, pp. 1249-1255.
8. *Atomization of Wall-Bounded Two-Phase Flows.* **Lightfoot, M. D. A.** Toronto, Canada : s.n., May 2006. ILASS Americas, Proceedings of the 19th Annual Conference on Liquid Atomization and Spray Systems.
9. *Internal Flow Effects in Prefilming Airblast Atomizers: Mechanisms of Atomization and Droplet Spectra.* **Sattelmayer, T. and Wittig, S.** 1986, Journal of Engineering for Gas Turbines and Power, Vol. 108, pp. 465-472.
10. *Motion and Evaporation of Shear-Driven Liquid Films in Turbulent Gases.* **Wittig, S., et al.** 1992, Journal of Engineering for Gas Turbines and Power, Vol. 114, pp. 395-400.
11. *Experimental and Numerical Studies of Evaporating Wavy Fuel Films in Turbulent Air Flow.* **Himmelsbach, J., Noll, B. and Wittig, S.** 1994, International Journal of Heat and Mass Transfer, Vol. 37, pp. 1217-1226.
12. **O'Rourke, P. J. and Amsden, A. A.** A Particle Numerical Model for Wall Film Dynamics in Port-Injected Engines. *SAE 961961*. s.l. : Society of Automotive Engineers, 1996.

13. *Liquid Film Atomization on Wall Edges - Separation Criterion and Droplets Formation Model*. **Maroteaux, F., et al.** 2002, Journal Of Fluids Engineering, Vol. 124, pp. 565-575.
14. *Potential of Inertial Instabilities for Fuel Film Separation in Port Fuel Injection Engine Conditions*. **Maroteaux, F., et al.** 2003, International Journal of Engine Research, Vol. 4, pp. 11-26.
15. *Comments on "Liquid Film Atomization on Wall Edges - Separation Criterion and Droplets Formation Model"*. **Gubaidullin, A.** 2007, Journal of Fluids Engineering, Vol. 129, pp. 665-666.
16. *Experimental Investigations of Liquid Film Stripping at a Sharp Corner*. **Steinhaus, B. C., Ghandhi, J. B. and Shedd, T. A.** Chicago, IL : s.n., May 2007. ILASS Americas, Proceedings of the 20th Annual Conference on Liquid Atomization and Spray Systems.
17. *The Flow of Thin Liquid Films Around Corners*. **Owen, I. and Ryley, D. J.** 1985, International Journal of Multiphase Flow, Vol. 11, pp. 51-62.
18. *Development of a Film Thickness Probe Using Capacitance for Asymmetrical Two-Phase Flow with Heat Addition*. **Klausner, J., Zeng, L. and Bernhard, D.** 1992, Review of Scientific Instruments, Vol. 63, pp. 3147-3152.
19. *Parametric Effects on the Void Fraction Measurement by Capacitance Transducers*. **Chun, M. H. and Sung, C. K.** 1986, International Journal of Multiphase Flow, Vol. 12, pp. 627-647.
20. *Film Thickness Measurements in a Simplex Swirl Atomizer*. **Suyari, M. and Lefebvre, A. H.** 1986, Journal of Propulsion and Power, Vol. 2, pp. 528-533.
21. *Local Film Thickness and Temperature Distribution Measurement in Wavy Liquid Films with Laser-Induced Luminescence Technique*. **Schagen, A. and Modigell, M.** 2007, Experiments in Fluids, Vol. 43, pp. 209-2221.
22. *Flourescence-Based Method Designed for Quantitative Measurement of Fuel Film Thickness During Cold-Start Engines*. **Yang, J. and Melton, L. A.** 2000, Applied Spectroscopy, Vol. 54, pp. 565-574.
23. *Thin Flowing Liquid Film Thickness Measurement by Laser Induced Fluorescence*. **Driscoll, D. I., Schmitt, R. L. and Stevenson, W. H.** 1992, Journal of Fluids Engineering, Vol. 114, pp. 107-112.
24. **Shaw II, B. T., Hault, D. P. and Wong, W.** Development of Engine Lubricant Film Thickness Diagnostics Using Fiber Optics and Laser Fluorescence. *International Congress and Exposition - SAE 920651*. Detroit, MI : Society of Automotive Engineers, 1992.

25. *Development of a Laser Fluorescence Technique for Measuring Piston Ring Oil Film Thickness.* **Ting, L. L.** 1980, Journal of Lubrication Technology, Vol. 102, pp. 165-171.
26. *Measurement of Liquid Film Thickness Using a Laser Light Absorption Method.* **Mouza, A. A., et al.** 2000, Experiments in Fluids, Vol. 28, pp. 355-359.
27. *Real-time Wave-amplitude Spectrum Analyzer for Air-liquid Interfaces.* **Barter, J. D. and Lee, P. H. Y.** 1994, Applied Physics Letters, Vol. 64, pp. 1896-1898.
28. *Collocated and Simultaneous Measurement of Surface Slope and Amplitude of Water Waves.* **Barter, J. D., Beach, K. L. and Lee, P. H. Y.** 1993, Review of Scientific Instruments, Vol. 64, pp. 2661-2665.
29. *Optical Measurement of Liquid Film Thickness and Wave Velocity in Liquid Film Flows.* **Hurlburt, E. T. and Newell, T. A.** 1996, Experiments in Fluids, Vol. 21, pp. 357-362.
30. *Automated Optical Liquid Film Thickness Measurement Method.* **Shedd, T. A. and Newell, T. A.** 1998, Review of Scientific Instruments, Vol. 69, pp. 4205-4213.
31. *Microwave Method for Measurement of Liquid Film Thickness in Gas-liquid Flow.* **Roy, R., et al.** 1986, Review of Scientific Instruments, Vol. 57, pp. 952-956.
32. *Measuring Interfacial Waves on Film Flowing Down a Vertical Plate Wall in the Entry Region Using Laser Focus Displacement Meters.* **Takamasa, T. and Hazuku, T.** 2000, International Journal of Heat and Mass Transfer, Vol. 43, pp. 2807-2819.
33. *Optical Interferometry for Measuring Instantaneous Thickness of Transparent Solid and Liquid Films.* **Ohyama, T., et al.** 1988, Review of Scientific Instruments, Vol. 59, pp. 2018-2022.
34. *Improved Interferometer for Measuring Unsteady Film Thickness.* **Nosoko, T., Mori, Y. H. and Nagata, T.** 1996, Review of Scientific Instruments, Vol. 67, pp. 2685-2690.
35. *Application of Laser Interferometry for Transient Film Thickness Measurements.* **Kelly-Zion, P., Collins, W. and Glawe, D.** Charlotte, NC : American Society of Mechanical Engineers, 2004. Proceedings of the 2004 ASME Heat Transfer/Fluids Engineering Summer Conference.

VITA

Mark Allan Friedrich was born in Lexington, Missouri on January 16, 1979. Mark graduated from Lexington High School in May of 1997 and enrolled in the John Deere Ag Tech program at Southeast Community College in Milford, Nebraska in July of 1997. He participated in the cooperative training program by working for Anson Implement, Inc. in Higginsville, Missouri (a John Deere dealer) as a service technician for a total of three terms. In March 1999, he graduated with distinction from SCC with an Associate of Applied Science in Transportation degree, receiving the Distinguished Graduate Award. From March 1999 to July 2001, Mark continued to work for Anson Implement, Inc. as a fulltime agriculture equipment service technician, specializing in electrical systems, air conditioning, hydraulics, and engine diagnostics and repair.

In the fall of 2001, Mark went back to school fulltime and enrolled in the engineering program at Longview Community College in Lee's Summit, Missouri. While there he worked part-time as a tutor in the Learning Assistance Center at LVCC as well as at the John Deere Parts Distribution Center in Kansas City, Missouri. In the spring of 2004, Mark was awarded the 2003-2004 Math, Science, and Engineering Student of the Year Award from Longview Community College.

In the fall of 2004, Mark transferred to the University of Missouri – Rolla and enrolled in the Mechanical Engineering program at UMR. While at UMR, he was involved in the American Society of Mechanical Engineers as well as the Mechanical Engineering Honor Society, Pi Tau Sigma, along with the Phi Theta Kappa International Honor Society. During his undergraduate career, he also worked in the Internal Combustion Engine Lab as an undergraduate research assistant under Dr. James Drallmeier and worked for John Deere Power Systems in Waterloo, Iowa in the summer intern program in 2005. In May of 2006, Mark received a Bachelor of Science degree in Mechanical Engineering from UMR and began work on his Master of Science degree in Mechanical Engineering under the advisement of Dr. James A. Drallmeier. After completing his Master of Science degree in May of 2008 from the Missouri University of Science and Technology (formerly UMR), Mark will begin work with John Deere Power Systems at the Product Engineering Center in Waterloo, Iowa as a member of the Engineering Development Program.

